Uranium and thorium partitioning in the bulk silicate Earth and the oxygen content of Earth's core

P. Faure, Mohamed Ali M.A. Bouhifd, M. Boyet, Geeth Manthilake, V. Clesi, J.-L. Devidal

Uranium and thorium partitioning in the bulk silicate Earth and the oxygen content of Earth's core

P. Faure[1*], M.A. Bouhifd[1], M. Boyet[1], G. Manthilake[1],

V. Clesi[1] and J.-L. Devidal[1]

[1]Laboratoire Magmas et Volcans, Université Clermont Auvergne, CNRS UMR 6524, OPGC-IRD, F-63000 Clermont-Ferrand, France

*Corresponding author: pierre.faure@etu.uca.fr

Abstract

This study investigates the partitioning of U and Th between molten metal and silicate liquid (D_U and D_{Th}) during Earth's core-mantle differentiation. We report new Th partition coefficients between chondritic silicate melt and various Fe-rich alloys in the system Fe-Ni-C-S-Si as determined by experiments in a multi-anvil apparatus at 3–8 GPa, 2073–2373 K, and oxygen fugacities from 1.5 to 5 log units below the iron-wüstite (IW) buffer. By compiling all existing data on molten metal-silicate liquid partitioning of U and Th, we develop global models of U and Th partitioning between the mantle and core throughout Earth's accretion. The calculated concentrations in the Bulk Silicate Earth (BSE) are in agreement with previous studies (U_{BSE} = 11.42 ± 0.45 ppb and Th_{BSE} = 43.20 ± 1.73 ppb), whereas the contents of these radioactive elements in the Earth's core remain negligible. Compared to recent geochemical estimations, the calculated $(Th/U)_{BSE}$ supports EL rather than EH enstatite chondrites as the reduced building blocks of the Earth. Furthermore, we demonstrate that Th is much more sensitive than U to the oxygen content of the metallic phase. To reproduce the Th/U ratio of the BSE within its uncertainties, the oxygen content of the Earth's core must be lower than 4.0 wt%. By

combining other existing constraints, this suggests that the core contains 2.0–4.0 wt% O. The calculations of U and Th concentrations and Th/U in the BSE developed herein can be used as new constraints for determining the concentrations of other refractory lithophile elements in the BSE as soon as their metal-silicate partition coefficients are well constrained over the conditions of core segregation.

1. Introduction

Uranium and thorium are refractory elements that condensed from the solar nebula at high temperatures (>1400 K). One would thus assume that the Th/U ratio in the bulk silicate Earth (BSE) should be equal (to the first order) to that of chondrites if these elements were not fractionated during Earth's core formation. However, existing geochemical models show some discrepancies between the U and Th concentrations and Th/U ratio of the BSE compared to those of chondrites, as well as large uncertainties. For instance, Lyubetskaya and Korenaga (2007) show a relative depletion of refractory lithophile elements compared to previous estimates (*e.g.*, McDonough and Sun, 1995; Palme and O'Neill, 2003). The BSE composition can be constructed using a geochemical approach based on mantle peridotite samples, which originate at depths shallower than the transition zone. In addition, model of the primitive mantle based on petrological data assumes global-scale homogeneity of the Earth's mantle. Moreover, the Th/U ratio of the upper mantle may have evolved with time due to changes in surface redox conditions. The recycling of U from the surface into Earth's interior differs from that of Th because U exists in two valence states (4+ and 6+), and highly soluble U^{6+} dominates under oxidized surface conditions. The terrestrial upper mantle sampled by mid-ocean ridge basalts shows a low Th/U ratio relative to that estimated from chondrites (Jenner and O'Neill, 2012; Gale et al., 2013). Indeed, the significant addition of recycled uranium into the upper mantle has been confirmed by high-precision $^{238}U/^{235}U$ measurements (Andersen et al., 2015).

The partitioning of radioactive elements between different Earth reservoirs is a topic of much debate since they play a major role in the thermal evolution of the Earth

and its mantle dynamics. Indeed, some amount of radioactive heating is necessary to drive the early geodynamo. Moreover, several studies have recently proposed that U and Th become more siderophile and/or chalcophile under reducing conditions, and consequently could have been sequestered in non-negligible amounts (up to 10 ppb U and 21 ppb Th) in the Earth's core (*e.g.*, McCubbin et al., 2012; Blanchard et al., 2017; Chidester et al., 2017; Wohlers and Wood, 2015, 2017, and references therein). It is thus essential to determine the budget of heat-producing elements in different planetary reservoirs.

In the present study, we present experimentally determined Th metal-silicate partitioning data at up to 8 GPa, 2373 K, and over a wide range of oxygen fugacity conditions and chemical compositions of the silicate and metallic phases, based on new chemical analyses of the experimental products reported in Bouhifd et al. (2013). The metal-silicate partitioning of Th has been the subject of very few experimental studies, and the only existing data were obtained at 1.5 GPa using mainly sulfide liquids (Murrell and Burnett, 1986; Wohlers and Wood, 2015, 2017). The**n,** we compiled all published experimental results on metal-silicate partitioning of these elements $D_{\mathrm{M}} = \frac{X_{\mathrm{M}}^{\mathrm{met}}}{X_{\mathrm{M}}^{\mathrm{sil}}}$ (where $X_{\mathrm{M}}^{\mathrm{met}}$ and $X_{\mathrm{M}}^{\mathrm{sil}}$ are the wt% concentrations of element M in the metal and silicate phases, respectively). It is then possible to regress these data to better constrain the influence of physical parameters (pressure, temperature, oxygen fugacity) and the chemical compositions of the studied phases on D_{U} and D_{Th}. These models were subsequently used to derive the U and Th concentrations in the BSE and the core as well as the Th/U ratio of the BSE, and our results are consistent with previous results (*e.g.*, Allègre *et al*., 2001; Kargel and Lewis, 1993; Lyubetskaya and Korenaga, 2007; and references therein). We combined our results with recent lead isotopic analyses (Wipperfurth *et al*., 2018) to

discriminate between different scenarios regarding Earth's building blocks. Furthermore, our models show also that the concentrations of U and Th in the Earth's core are less than 1.5 ppb and 5 ppb, respectively. Finally, the calculations performed herein provide new constraints on the oxygen content of the core, which cannot exceed 4 wt%.

2. Experimental methods

The run-products used in the present study are those described and analysed in Bouhifd *et al*. (2013). Here, we report new chemical analyses of thorium in the silicate and metallic phases and of oxygen in the Fe-rich alloys. In the following, we briefly summarize the experimental procedure and fully describe the analytical methods used to derive our new results.

2.1. Starting materials

Silicate starting materials consisted of a C1-chondrite model composition containing 49.6 wt% SiO_2, 35.1 wt% MgO, 8.5 wt% FeO, 3.5 wt% Al_2O_3, and 3.3% CaO (Wasson and Kallemeyn, 1988). This silicate composition is similar to that used to determine the effect of water on the behavior of siderophile elements during core formation (*e.g.*, Clesi *et al*., 2016). Doping was achieved with mixtures of U and Th dissolved in 0.5 M nitric acid (AAS standard solutions), which was denitrified in air at 1100 K for 4 h. The doping mixtures were added to the silicate starting material to achieve concentrations of 1000 to about 4000 ppm per element. Fe-rich alloy powders in the Fe–Ni–Si–S system were added to the silicate starting material in 50:50 proportions by weight to obtain several starting compositions. Oxygen fugacity (fO_2) was varied between IW –

2 and IW –5 by adding metallic Si to the starting material. Each starting composition was then mixed and ground under ethanol, and dried at ~400 K for at least 24 h.

2.2. High-pressure and high-temperature syntheses

The high-pressure and high-temperature experiments were performed by Bouhifd *et al*. (2013) using the French national 1000-ton and 1500-ton multi-anvil facilities in Clermont-Ferrand, France. Briefly, the pressure assembly consisted of Cr-doped MgO octahedra (18 or 14 mm edge length) containing a $LaCrO_3$ heater. The octahedra were compressed using 32 mm tungsten carbide anvils with truncation edge lengths of 11 and 8 mm for the 18 and 14 mm octahedra, respectively, and pyrophyllite gaskets. Samples were contained in either graphite or MgO single-crystal capsules in order to test the impact of the capsule material on the measured metal-silicate partition coefficients. The samples were first compressed to the desired pressure at room temperature (for instance for 5 GPa experiments, we use about 100 tons on a 14/8 assembly) and then heated to the target temperature for run durations of 1 to 2 min. These durations are sufficient to achieve equilibrium between silicate melt and metallic liquid as found for many other studies (*e.g.*, Corgne *et al*. 2008; Cartier *et al*., 2014; Bouhifd *et al*., 2015; Clesi *et al*., 2018; and references therein) and short enough to prevent excessive reaction between the capsule and the silicate or metallic phases. Temperatures were monitored with a thin axial $W_5Re/W_{26}Re$ thermocouple whose junction was in direct contact with the top of the capsule. The thermocouples presented no difference of behavior when using either graphite or MgO single crystal capsule, showing the non-contamination of thermocouple during graphite experiments. The pressure and temperature uncertainties are estimated to

be ±1 GPa and ±100 K, respectively. The samples were quenched by shutting off the power, which resulted in an initial quench rate of approximately 800 K/s. The samples were then decompressed over about 12 h. After the completion of each experiment, the run product was mounted in epoxy, polished, and carbon coated for chemical analyses.

2.3. Electron Microprobe

The major and minor element compositions of the metal and silicate phases were analyzed with a CAMECA SX100 electron microprobe with a 20 kV accelerating voltage at the Laboratoire Magmas et Volcans (LMV, Clermont-Ferrand, France). Major element analyses in silicate phases were performed at 50 nA with a 10–20 μm defocused beam, with on-peak counting times ranging from 5 to 80 s depending on element concentrations and detection limit requirements (*e.g*. Bouhifd *et al*., 2013). Wollastonite was used as a standard for Si and Ca, and MgO, Al_2O_3, and Fe_2O_3 for Mg, Al, and Fe, respectively. To analyze K and S, we used natural $KAlSi_3O_8$ and ZnS as standards, respectively. For metallic phase analyses, we used a defocused beam (10–20 μm), beam currents of 15 nA for major elements (Fe, Ni, and Si) or 150 nA for trace elements, and on-peak counting times ranging from 5 to 60 s. Pure Ni, Si, and Fe metals were used as standards. For samples embedded in graphite capsules, we estimated the carbon content of the Fe-alloys from the deviation of the analytical totals from 100%.

In the present study, we essentially focused our chemical analyses to determine the concentrations of Th in the silicate phase and oxygen contents in the metal phases. To analyze Th in the silicate, thorianite (ThO_2) was used as standard. For metal analyses, pure Ni, Si, and Fe (NIST 665) metals were used as standards. To analyze oxygen in

147 metallic phases, NIST 665 and Fe_2O_3 were used as standards. Prior to analyses, the
148 samples and standards were polished and carbon coated in the same way, then kept under
149 vacuum until analysis. Analyses were performed using 20 kV accelerating voltage, a
150 beam current of 15 nA, and a defocused beam of 30 μm, and the detection limit for oxygen
151 in the metals was 550 ppm.

152 During the oxygen analyses, we found that the nominally oxygen-free standards
153 contained about 0.21 ± 0.02 wt% O at 20 kV accelerating voltage; this value was
154 consistent among the standards. We additionally observed that the measured oxygen
155 contents of the standards decreased with increasing voltage from 7 to 15 kV before
156 reaching a plateau between 15 and 25 kV (the maximum voltage tested). We concluded
157 that the measured oxygen contents in the O-free standards were the result of rapid
158 adsorption of oxygen onto the surface of the standards. Therefore, we subtracted the value
159 obtained from the standards at 20 kV from every analysis of our run-products. The
160 corrected concentrations are presented in Tables A1 and A2. The reported oxygen
161 analyses are in good agreement with the recent parameterization for metal-silicate oxygen
162 partitioning reported by Fischer *et al*. (2015).

163

164 **2.4. LA-ICP-MS**

165 U and Th concentrations in both metal and silicate phases were analyzed by laser
166 ablation inductively coupled plasma mass spectrometry (LA-ICP-MS) at LMV. We used
167 a quadrupole ICP-MS (Agilent 7500-cs, Agilent Technologies) coupled with a 193 nm
168 ArF excimer-type laser (Resonetics M-50). The laser was fired on selected sample regions

169 at a repetition rate of 3 Hz with 8 mJ output and a spot size of 15–44 μm. Pit depths were
170 roughly equivalent to the spot size.
171 During LA-ICP-MS analyses, the Ca signal was monitored during metal analyses
172 and the Fe and Ni signals during silicate analyses. Any sudden variation of their contents
173 was indicative of phase contamination (*i.e.*, metal contamination during silicate phase
174 analysis or vice versa). Ablation was performed under a pure He flow for durations of
175 about 80 s (blank count rates were measured for 20 s prior to 60 s of ablation). The analyte
176 was carried to the ICP torch by a gas mixture in which N_2 + Ar gases were added to the
177 pure He gas. Reference glasses NIST SRM 610, NIST 612, and BCR2-G were used for
178 external calibration (Gagnon et al., 2008), and ^{29}Si, ^{57}Fe, and ^{60}Ni were used for internal
179 calibration. All data were processed using the GLITTER software package (Achterberg
180 et al., 2001). Detection limits calculated for U and Th were below 1 ppm.
181

182 **3. Results**

183 The experimental conditions and calculated U and Th partition coefficients (D_U and
184 D_{Th}, respectively) are summarized in Table 1, and the chemical compositions of the
185 quenched silicate and metallic melts are reported in Tables A1 and A2. Typical run
186 products contained two immiscible phases: silicate glass and Fe-rich alloy (Fig. 1).
187 Microstructures of the run products showed that both phases were fully molten during the
188 experiments. In some cases, we observed dendritic microstructures in the silicate. When
189 dendritic microstructures were present within the region of interest, LA-ICP-MS analyses
190 were performed using a 44 μm spot size to average the heterogeneous quenched texture.
191 Several criteria indicate the attainment of thermodynamic equilibrium in these

192 experimental samples: (i) multiple analyses in the silicate phase show that it is
193 homogeneous with no evidence of chemical zoning, and (ii) all metal blobs embedded in
194 the silicate matrix are of similar composition.

195 A critical parameter during metal-silicate partitioning using the multi-anvil
196 technique is the nature of the capsule, because no material can be completely inert to both
197 silicate and metal liquids. Here we used two different capsules: MgO single-crystal and
198 graphite capsules. Using graphite capsules, we usually observed low analytical totals for
199 the metallic phase, *i.e.*, between 93 and 98.9 wt% (Table A1), indicating significant
200 amounts of carbon dissolved in the Fe-rich alloy. However, we did not observe any effect
201 of the capsule material on D_U or D_{Th} considering analytical errors over the range of *P-T*
202 conditions explored in this study (Fig. 2). Similar behavior has been observed for the
203 metal-silicate partition coefficients of U and other lithophile elements (Bouhifd *et al.*,
204 2013; 2015; and references therein). Finally, our experimental results showed that varying
205 the concentrations of U and Th in the starting materials had no effect on the resulting
206 metal-silicate partition coefficients (Tables A1 and A2).
207

208 **3.1 Oxygen fugacity**

209 The prevailing oxygen fugacities in our experiments were calculated based on the
210 Fe and FeO contents of the quenched metal and silicate phases, respectively, by
211 considering the equilibrium reaction between Fe metal and Fe oxide:

212 $$Fe^{metal} + ½\ O_2 \leftrightarrow FeO^{silicate} \quad (1)$$

213 The fO_2 can thus be estimated relative to the Iron-Wüstite buffer (IW) from the activities
214 of Fe in the metal and FeO in the silicate following the equation:

$$\log fO_2(\Delta IW) = 2\times\log\left(\frac{a_{FeO}^{sil}}{a_{Fe}^{met}}\right), \quad (2)$$

where $a_{FeO}^{sil} = \gamma_{FeO}^{sil} \times X_{FeO}^{sil}$ and $a_{Fe}^{met} = \gamma_{Fe}^{met} \times X_{Fe}^{met}$ represent the activities of FeO in the silicate liquid and Fe in the metal, respectively, γ_{FeO}^{sil} and γ_{Fe}^{met} are their respective activity coefficients, and X_{FeO}^{sil} and X_{Fe}^{met} their respective mole fractions.

We calculated the activity coefficient of Fe in the Fe-rich alloys based on the formula of Ma (2001) using the interaction parameters ε defined in the Steelmaking Data Sourcebook (1988) (see also Wade and Wood, 2005; Siebert *et al*., 2011) by the following formula for metallic solutions containing N components (six in our study: Fe, Ni, O, S, C and Si):

$$\ln\gamma_{Fe} = \sum_{i=1}^{N-1}\varepsilon_i^i(\chi_i + \ln(1-\chi_i))$$

$$-\sum_{j=1}^{N-2}\sum_{k=j+1}^{N-1}\varepsilon_j^k\,\chi_j\chi_k\left(1+\frac{\ln(1-\chi_j)}{\chi_j}+\frac{\ln(1-\chi_k)}{\chi_k}\right)$$

$$+\sum_{i=1}^{N-1}\sum_{k=1(k\neq 1)}^{N-1}\varepsilon_i^k\,\chi_i\chi_k\left(1+\frac{\ln(1-\chi_k)}{\chi_k}-\frac{1}{1-\chi_i}\right)$$

$$+\frac{1}{2}\sum_{j=1}^{N-2}\sum_{k=j+1}^{N-1}\varepsilon_j^k\,\chi_j^2\chi_k^2\left(\frac{1}{1-\chi_j}+\frac{1}{1-\chi_k-1}-1\right)$$

$$-\sum_{i=1}^{N-1}\sum_{k=1\,(k\neq i)}^{N-1}\varepsilon_i^k\,\chi_i^2\chi_k^2\left(\frac{1}{1-\chi_i}+\frac{1}{1-\chi_k}+\frac{\chi_i}{2(1-\chi_k)^2}-1\right) \quad (3)$$

This treatment is available using the activity calculator (http://www.earth.ox.ac.uk/~expet/metalact/) provided by the university of Oxford

(Wade and Wood, 2005). No pressure correction is made in our calculations due to the lack of reliable data for all elements.

To determine $\gamma_{\mathrm{FeO}}^{\mathrm{sil}}$ for all silicate melt compositions, we used the average value ($\gamma_{\mathrm{FeO}}^{\mathrm{sil}} = 1.5 \pm 0.5$) derived from studies at 1 bar by O'Neill and Eggins (2002) for several melt compositions in the CaO-MgO-Al_2O_3-SiO_2 system, and by Holzheid et al., (1997) for melts in the anorthite-diopside system and komatiitic basalt, assuming no pressure effect (Toplis, 2004). The calculated fO_2 of our experiments ranged from IW –5 to IW –1. Values determined for each experiment are reported in Tables A1 and A2. For comparison, we also report the value of fO_2 calculated assuming ideality ($\gamma_{\mathrm{FeO}}^{\mathrm{sil}} = \gamma_{\mathrm{Fe}}^{\mathrm{met}} = 1$), and the difference between the two values is within the uncertainties of the calculations. Thus, in the following, we use the fO_2 values calculated for the non-ideal system.

3.2. Parameterizations of the result

As reported in previous studies (*e.g.*, Righter *et al.*, 1997), the metal-silicate partition coefficient of element M ($D_{\mathrm{M}}^{\mathrm{met/sil}}$) is linked to the free energy of the reaction, and can be related to T, P, and fO_2 by the following equation, to which we have added three terms to account for the metal composition (here, the silicate composition was kept constant, reflecting the early mantle during core formation):

$$\log\left(D_{\mathrm{M}}^{\mathrm{met/sil}}\right) = a\log(fO_2) + b\frac{1}{T} + c\frac{P}{T} + d\log(1 - X_{\mathrm{S}}^{\mathrm{met}}) + e\log(1 - X_{\mathrm{Si}}^{\mathrm{met}}) + f\log(1 - X_{\mathrm{O}}^{\mathrm{met}}) + cst, \quad (4)$$

where a is related to the valence of element M in the silicate melt, and b and c are related to the enthalpy $\left(\frac{\Delta H^\circ}{RT}\right)$ and volume $\left(\frac{P\Delta V^\circ}{RT}\right)$ of the system, respectively. Parameters d, e, and f are constants related to the chemical composition of the metallic phase. The term *cst* includes the effect of the entropy of the system $\left(\frac{\Delta S^\circ}{R}\right)$.

Using all existing data (presented here along with published data) for molten metal-silicate liquid partitioning of U (63 data points) and Th (32 data points) for which the T, P, fO_2, and silicate and metal compositions are all well characterized, we refined the coefficients in equation (4) by multiple linear regression following a previously validated approach (Bouhifd *et al*., 2013; Righter and Drake, 2003; Righter *et al*., 2010). Data available in the literature come from a variety of sources (detailed in Appendix B) using a variety of synthesis techniques presenting consistent results: piston-cylinder, multi-anvil cell as well as diamond anvil cell. In order to obtain the best-fit parametrizations, we excluded experiments with high uncertainties (>75% of the reported partition coefficients), and data involving liquid metal-solid silicate equilibrium considered as irrelevant to magma ocean conditions. For consistency, the literature values for fO_2 and partition exchange coefficients were recalculated using the reported concentrations of each element.

To determine the best-fit solutions for U and Th using equation (4), we performed several tests to establish the robustness of these parameterizations (Appendix C). The resulting parametrizations succeed in reproducing the experimental partition coefficients for a given set P, T, fO_2 and chemical composition (Fig. 3a, b), and will thus be used to

discuss the behavior of U and Th as a function of P, T, fO_2, and the chemical composition of the core.

3.2.1. Effects of pressure and temperature on D_U and D_{Th}

The first test of our parameterizations of the metal-silicate partitioning of U and Th show that, within the range of experimental conditions investigated, the pressure has only negligible effects on D_U and D_{Th}. For instance, at ΔIW –2 and constant chemical composition of the metallic phase (79.5 wt% Fe, 10 wt% Ni, 6 wt% Si, 2.5 wt% O, 2 wt% S), the effect of pressure on D_U is relatively small. Varying the pressure from 10 to 50 GPa (at 3500 K) lead to a small variation of D_U from about 5×10^{-3} to 8×10^{-3}. However, data for Th are only available up to 8 GPa. By plotting the D_{Th}/D_U ratio versus pressure (Fig. 4), we found that this ratio is constant within uncertainties. So we set the parameter c (related to the pressure in equation (4)) to zero. By doing so, we found that the quality of subsequent parameterizations with $c = 0$ is unchanged (Appendix C).

At constant pressure (between 5 and 50 GPa), a temperature increase from 2500 to 3500 K induces an increase of D_U and D_{Th} of about one order of magnitude. This suggests that, of the two parameters, temperature is the factor that most strongly influences the molten metal-silicate liquid partitioning of U and Th, consistent with results for U reported by Chidester *et al*. (2017).

3.2.2. Oxidation state of U and Th at reducing conditions

Metal-silicate partitioning experiments can be used to estimate the valence of any metallic element M in a silicate liquid as function of fO_2. The partitioning of an element

M between silicate and metal involves an exchange reaction between its oxidized form ($MO_{n/2}$) in the silicate melt and its reduced form in the metal (M), which depend on fO_2 and the valence n of the element in the silicate as reported in the following reaction:

$$MO_{n/2} \leftrightarrow \frac{n}{4}O_2 + M \quad (5)$$

It is therefore possible to interpret the parameter a of our multi parameter linear regression as equal to $-\frac{n}{4}$ for each element. From equation (4), we determined that parameter a for thorium is –0.95 ± 0.25, consistent with its valence of 4+ in silicate melts at reducing conditions from ΔIW –5 to ΔIW –1. However, for uranium, we determined parameter a to be –0.73 ± 0.09, indicating a more complicated exchange reaction than for Th. Previous studies have proposed that the valence of U in silicate melts under reducing conditions can be 4+, as suggested by low pressure (<20 GPa) metal-silicate partitioning experiments (*e.g.* Malavergne *et al.*, 2007; Bouhifd *et al.*, 2013; Wohlers and Wood, 2017), or 2+ (*e.g.* Chidester et al., 2017; Blanchard et al., 2017; Boujibar et al., 2019). The parameterization performed herein shows that the parameter a for U does not correspond to any single valence state (4+ or 2+). By fixing the parameter a to –1 or to –0.5, reflecting a valence of 4+ or 2+ for uranium in silicate melts at reducing conditions, the quality of our parameterizations remains the same as for a = –0.73. So we decided to keep this parameter equals to –0.73 ± 0.09 avoiding any supplementary hypothesis on the parameterizations. In fact, when we report the uranium partition coefficients as a function of oxygen fugacity for experiments where the S content is low (X_S < 2 wt%), we could see a change of the valence of U in silicate melt from 4+ to 2+ around ΔIW -2 (Fig. 5). This behavior is consistent with the change of the oxidation state of Nb and Ta in silicate melts at reducing conditions (Cartier *et al.*, 2014). However, further experiments and X-

ray absorption near edge structure analyses are required to confirm and better characterize the valence of uranium in silicate melts at the conditions of Earth's core formation.

3.2.3. Effects of silicate and metal compositions on D_U and D_{Th}

The existing data on molten metal-silicate liquid partitioning of uranium show disagreement about the effect of silicate composition on D_U. Chidester *et al*. (2017) proposed that the SiO_2 content of the silicate has a measurable effect on D_U. However, Blanchard *et al*. (2017) found that there is no effect of the SiO_2 content nor the degree of polymerization of the silicate melt on D_U. By combining all existing data on molten metal – silicate liquid partitioning of U and Th we found that the effect of SiO_2 has no significant impact on the partitioning of Th and U (see Appendix C).

The effect of carbon dissolved in the metallic phase on D_U and D_{Th} is estimated by comparing C-bearing and C-free experiments. As reported in Tables A1 and A2, the presence of carbon in the metallic phase has only a negligible impact on D_U and D_{Th} (Fig. 2). This is in good agreement with the C-U interaction parameter in a C-saturated iron alloy, listed as 0 at temperatures around 1600–1700 K in the Steelmaking Data Sourcebook (1988). Thus, since we do not observe any significant impact of carbon (up to 4.8 wt%) on D_U and D_{Th} (Fig. 2), we do thus not include a parameter for C in our parameterizations for U and Th.

We also found that varying the Si content of the metallic phase did not lead to significant variations of the Th/U ratio of the BSE nor concentrations of U and Th in the different reservoirs. For example, an accretion scenario with a Si-free core and a scenario using the parametrization taken from Fischer *et al*. (2015) (which propose a core with 8.5

wt% Si) lead to a 1% variation of the Th/U ratio of the silicate reservoir when all other parameters are kept constant. So, we do not include a parameter for Si in our parameterizations.

The effect of sulfur in the metallic phase on D_U and D_{Th} seems to depend on S concentration and experimental pressure. For instance, we noticed a small dependence of D_U and D_{Th} on S content for concentrations <10 ± 2 wt%; D_U and D_{Th} increase by less than half an order of magnitude when the S content is increased from 2 to 10 wt%, consistent with low-pressure (Fig. 6) and high-pressure experimental data (*e.g*. Bouhifd *et al*., 2013; Blanchard *et al*., 2017; Chidester *et al*., 2017). However, we observed a strong dependence of D_U and D_{Th} on S concentrations at >20 wt% S. At low pressures (<20 GPa) and ΔIW –2, increasing the sulfur content from 2 to 35 wt% (corresponding to the FeS composition) results in an increase of D_U from 8.4×10^{-4} to 4.4×10^{-1} (roughly three orders of magnitude), and D_{Th} shows a smaller variation from 8.4×10^{-4} to 8.3×10^{-2}. At higher pressures (around 50 GPa), 3000 K, and ΔIW –2, increasing the S content from 2 to 35 wt% led to an increase of D_U from about 4.6×10^{-3} to 2.4, making U a slightly siderophile element at these extreme conditions. At the same conditions, the same increase in S content increases D_{Th} from 6.2×10^{-3} to 0.6; Th thus remains a lithophile element at all investigated P, T, and fO_2 conditions and chemical compositions. We note that for sulfide-silicate partitioning at ΔIW –2, D_U is ~10 times higher than D_{Th}. Similar conclusions were made by Wohlers and Wood (2017) from low-pressure and low-temperature data. However, at lower oxygen fugacities around IW –5, they differ by only a factor of 2.

By performing the parameterizations presented herein, we found the oxygen content of the metallic phase to exert the strongest influence on metal-silicate U and Th partitioning. D_{Th} is more sensitive than D_U to the oxygen content of the metal. For instance, at similar *P-T* conditions and ΔIW –2, an increase in the oxygen content of the metal from 2 to 5 wt% increases D_U by less than one order of magnitude (from ~5×10^{-4} to 3×10^{-3}) but D_{Th} by about two orders of magnitude (from ~2×10^{-4} to 1.7×10^{-2}). This difference will provide strong constraint on the composition of the Earth's core, as discussed in section 4.2.

Finally, we note that we were able to separate the effects of oxygen and sulfur on D_U and D_{Th} by compiling all existing data from S-rich systems at low pressures to S-free systems at high pressures, as S-rich and S-free metals are known to incorporate oxygen at low and high pressure, respectively. For example, whereas Blanchard *et al*. (2017) used only high-pressure experiments to constrain the impact of O on metal-silicate U partitioning, our parameterization incorporates data from S-rich experiments at low pressure (Wohlers and Wood, 2015, 2017) and S-free to S-rich experiments at high pressure (Blanchard *et al*., 2017; Chidester *et al*., 2017).

By taking into account all the features discussed above, the best-fit solutions of our parameterizations for molten metal – silicate liquid partitioning of uranium and thorium are reported in equations (6) and (7). These equations will be used to discuss the behavior of U and Th during the Earth's core segregation.

$$\log\left(D_U^{met/sil}\right) = (-0.72 \pm 0.07) \times \log(fO_2) + (-8346 \pm 1804) \times \frac{1}{T} + (-15.33 \pm 1.13) \times \log(1 - X_S^{met}) + (-51.55 \pm 7.86) \times \log(1 - X_0^{met}) + (-1.52 \pm 0.52) \quad (6)$$

$$\log\left(D_{\mathrm{Th}}^{\mathrm{met/sil}}\right) = (-0.96 \pm 0.10) \times \log(fO_2) + (-9967 \pm 2618) \times \frac{1}{T} + (-13.76 \pm 1.40) \times \log(1 - X_{\mathrm{S}}^{\mathrm{met}}) + (-137.82 \pm 26.63) \times \log(1 - X_{\mathrm{O}}^{\mathrm{met}}) + (0.77 \pm 1.12) \quad (7)$$

Where $D_{\mathrm{U}}^{\mathrm{met/sil}}$ and $D_{\mathrm{Th}}^{\mathrm{met/sil}}$ are molten metal – silicate liquid partition coefficients of uranium and thorium (on weight basis), respectively; f_{O2} is the oxygen fugacity relative to the iron-wüstite buffer; T is the temperature in K; $X_{\mathrm{S}}^{\mathrm{met}}$and $X_{\mathrm{O}}^{\mathrm{met}}$ are the wt% contents of S and O in the metallic phase, respectively.

4. Discussion

4.1. U and Th concentrations and the Th/U ratio of the bulk silicate Earth

The U and Th contents of the BSE depend on the total amounts of both elements on Earth, which are directly connected to the nature of Earth's building blocks and their partitioning between silicate and metal reservoirs. Geochemical data from chondrites show that absolute U and Th concentrations both vary by about 23% among the different chondrite groups, whereas the Th/U ratio is relatively constant, varying by only 7% (Wasson and Kallemeyn, 1988). To reproduce the present-day mantle FeO content of about 8 wt%, the Earth must have been accreted from a large fraction (80–90%) of reduced bodies (EH or EL enstatite chondrites) with 10 to 20% of Earth's mass likely accreted from more oxidized bodies (*e.g.*, Clesi *et al*., 2016; Rubie *et al*., 2015). Furthermore, Dauphas *et al*. (2014) showed that the terrestrial ^{17}O, ^{48}Ca, ^{50}Ti, ^{62}Ni, and ^{92}Mo isotopic compositions can be reproduced by a mixture of 91% enstatite, 7%

ordinary, and 2% carbonaceous chondrites. Indeed, this chondritic composition can explain the subchondritic Nb/Ta ratio of the BSE (Cartier *et al*., 2014).

Similarly, we present here models of planetary accretion focusing on the evolution of the U and Th contents and the Th/U ratio of the BSE. We adopted continuous core formation models similar to those reported by Rubie *et al*. (2015) and Clesi *et al*. (2016). In our models, the Earth accreted from impactors of a given chemical composition, which then equilibrated (fully or partially) with the magma ocean of the proto-Earth until the planet obtained its final mass (M_E). We assume that impactors were already differentiated into silicate mantles and metallic cores (Taylor and Norman, 1990). This differentiation is defined by a pressure and temperature of equilibrium, leading to the partitioning of their bulk compositions coherent with their masses M_I (from 0.01 M_E to 0.1 M_E). This assumption only affects the results when the cores of impactors fail to completely equilibrate with the terrestrial magma ocean, which is predicted to have occurred only during the final few relatively large impacts (*e.g*. Deguen *et al*., 2014) (see below).

At each step of accretion (1% M_E), the impactor's metal and silicate equilibrate within the proto-mantle, which accounts for 68% of the planet's mass. We tested various increments of accretion (0.1%, 1%, and 10% M_E) and observed no impact on the final result as long as the ratio M_I/M_E is maintained. We set the equilibration pressure to 50% of the core-mantle boundary pressure at each step. This fraction is derived from previous studies on the partitioning of siderophile elements sensitive to pressure (*e.g.*, Boujibar *et al*., 2014; Fischer *et al*., 2015), leading to a final pressure of equilibration of 60 GPa (Siebert *et al*., 2012). Temperature is fixed at the liquidus of chondritic melts (Andrault et al., 2011), which evolved from 1900 K at 1% accretion to 3500 K during the final stage

435 of accretion. Oxygen fugacity is constrained by the building block composition and the
436 amount of reduced / oxidized building block along accretion. Since a large amount of
437 reduced bodies is required to meet Earth's isotopic composition (Dauphas et al., 2014;
438 Dauphas, 2017; Javoy, 2010; Boyet et al., 2018), this model follows the fO_2 paths defined
439 in Clesi *et al*. (2016), *i.e.*, ranging from IW –5 to IW –2. However, The fO_2 path of Earth
440 accretion has a negligible effect on the resulting $(Th/U)_{BSE}$ which vary by less than 0.7%
441 when considering an accretion at constant fO_2 (IW-2 throughout accretion) instead of a
442 reduced to oxidized accretion scenario. The fO_2 path mainly affects the content of the
443 metallic phase in light elements (see below). Partitioning is determined using our
444 parameterizations for U and Th (Table 2). Following the approach of Deguen *et al*.
445 (2014), we take into account the effect of partial metal-silicate equilibration on elemental
446 partitioning, which mainly affects the last 40% of Earth's accretion. We consider that
447 equilibration between the proto-Earth's mantle and the metal of the impactors becomes
448 less efficient as accretion progresses (*e.g.*, Deguen *et al*., 2014; Rubie *et al*., 2015). For
449 the last giant impact that formed the Moon ($M_I = 0.1\ M_E$), we find that the impactor's core
450 merges almost completely with the Earth's proto-core, with less than 5% of its mass
451 equilibrating with the silicate mantle. However, we find that the impact of this
452 equilibration on our parameterization is very limited, in agreement with Rudge *et al*.
453 (2010). Since we consider two mostly lithophile elements, disequilibrium models are as
454 compatible with the geochemical observations as equilibrium models, and the elemental
455 concentrations of the BSE remain within uncertainties in either case.

456 At each step of accretion, the O, Si, and Ni content of the metallic core is calculated
457 using the parameterization of Fischer *et al*. (2015). The C content of the core remains

458 constant at 0.2 wt% during accretion (Wood *et al*., 2006), and a late addition of sulfur-
459 rich material increases the S content of the core to 2 wt% to fit geophysical, geochemical,
460 and experimental estimates (*e.g.*, Allègre *et al*., 1995; Boujibar *et al*., 2014; Dreibus and
461 Palme, 1996; Palme and O'Neill, 2003). Variations of the O and Si contents in the metal
462 are related to the proportion of reduced and oxidized building blocks, which influence the
463 fO_2 path. At the end of accretion model in which Earth is built from a major proportion
464 (80%) of reduced materials, the Earth's core contains 0.2 wt% C, 2 wt% S, 6.75 ± 0.75
465 wt% Si, and 2.8 ± 0.7 wt% O. On the other hand, models in which Earth is built from
466 more oxidized materials (following an accretion with constant fO_2 at IW–2, Fischer *et al*.
467 (2015) and references therein) propose Earth's core concentrations up to 5.85 wt% O and
468 2.04 wt% Si. To determine the viability of any accretion scenarios and the resulting U
469 and Th concentrations in the different reservoirs, we also studied the evolution of Ni, Co,
470 Nb, and Ta, elements that have well-constrained metal-silicate partitioning behavior in
471 the literature. The parameterizations used to constrain the behaviors of these elements are
472 those of Fischer *et al*. (2015) for Ni and Co and Cartier *et al*. (2014) for Nb and Ta. As a
473 first test of validity, any accretion scenarios studied herein must reproduce the Ni/Co and
474 Nb/Ta elemental ratios in the present-day mantle.

475 A major contribution of enstatite chondrites during Earth's accretion is supported
476 by the strong similarities between mass-independent isotopic ratios measured in enstatite
477 chondrite and terrestrial samples (*e.g.*, Javoy, 1995; Dauphas, 2017; Boyet *et al*., 2018).
478 However, the most recently published trace element measurements of enstatite chondrites
479 (Barrat *et al*., 2014; Dauphas and Pourmand, 2015) reveal variable U and Th
480 concentrations and significant differences relative to the compilation published by

Wasson and Kallaymen (1988). As U and Th concentrations are low in enstatite chondrites, obtaining accurate measurements remains challenging. Thus, in our model, we consider the enstatite chondrite U and Th concentrations of Barrat *et al*. (2014) and Dauphas and Pourmand (2015) to represent the reduced end-members. We note here the significant effect of weathering on the Th/U ratios of samples reported in these studies. Under oxidizing surface conditions, these elements show contrasting behavior, with U behaving as a water-soluble hexavalent species, whereas Th remains in a tetravalent state (Kramers and Tolstikhin, 1997). Prolonged exposure to atmospheric conditions would therefore raise the Th/U ratio of extraterrestrial samples. For instance, the average Th/U ratios of enstatite chondrites (falls and finds) are 4.23 ± 0.81 for EL chondrites and 3.59 ± 0.52 for EH chondrites (1σ uncertainties), but these ratios are lowered to $(Th/U)_{EL}$ = 3.85 ± 0.52 and $(Th/U)_{EH}$ = 3.24 ± 0.21 when only chondrite falls are included. Therefore, we only took into account concentrations measured in chondrites fall (Table 3). Results published by Barrat et al. (2014) and Dauphas and Pourmand (2015) were obtained using classical ICPMS technique and isotope dilution by MC-ICPMS, respectively. Three samples (2 EL and 1 EH) are significantly different from the average Th/U values and have been removed from the dataset (see Appendix D). The average values are 4.39±0.52 and 3.24±0.17 for EL and EH groups, respectively. Identical values are obtained when only concentrations obtained by isotope dilution technique are considered.

We tested several scenarios involving different carbonaceous chondrites as the oxidized building blocks of the Earth. Scenarios 2, 6, 7, and 8 (Table 4) which involve different type of carbonaceous chondrites, show no significant differences in the final

504 concentrations of the modeled reservoirs. Therefore, we henceforth use CI chondrite falls
505 (Table 3) as a proxy for the oxidized building blocks as they have the most precisely
506 analyzed trace element concentrations (Barrat *et al*., 2012).

507 Table 4 summarize the results of several scenarios of Earth accretion involving
508 various building block mixing. All these scenarios reproduce the Nb/Ta and Ni/Co
509 elemental ratios of the BSE, within uncertainties, as shown in Table 4. Our calculations
510 produce a BSE with 11.77 ± 0.45 ppb U, 40.42 ± 1.62 ppb Th, and Th/U = 3.43 ± 0.13
511 when using only EH chondrites as the reduced material (scenario 1, Table 4), and
512 11.42±0.45 ppb U, 43.20±1.73 ppb Th, and Th/U = 3.78 ± 0.15 when using only EL
513 chondrites as the reduced material (scenarios 2, Table 4).

514 The same calculations show the Earth's core to contain about 1.28 ppb U and 4.80
515 ppb Th using EH chondrites (scenario 1) or 1.24 ppb U and 5.22 ppb Th using EL
516 chondrites (scenario 2). Such U and Th concentrations would produce much less than 1
517 TW of energy due to radioactive decay, compared to the estimated 5–15 TW heat flux
518 escaping the core (Lay *et al*., 2008). Thus, even for the highest D_U and D_{Th} values, the U
519 and Th contents of the Earth's core represent a negligible contribution to the heat flow
520 from the core to the mantle. These results are marginally affected by increasing the
521 amount of the reduced materials from 80 to 90% (scenarios 1, 2 and 9, Table 4).

522 Our results are also in agreement, within uncertainties, with the Th/U
523 concentrations reported by several authors (*e.g.*, Allègre *et al*., 2001; McDonough and
524 Sun, 1995; Kargel and Lewis, 1993; Lyubetskaya and Korenaga, 2007, and references
525 therein). However, given the large uncertainties on the published Th/U value of the BSE
526 (up to 35% of the reported value), it is not possible to discriminate between the different

527 scenarios proposed here. Nevertheless, Wipperfurth *et al*. (2018) recently proposed
528 $\mathrm{Th/U} = 3.776^{+0.122}_{-0.075}$ for the BSE, derived from the $^{208}Pb^*/^{206}Pb^*$ ratios (where the
529 asterisks denote the radiogenic component) of various terrestrial rocks compared to the
530 chondritic $^{208}Pb^*/^{206}Pb^*$ value (Blichert-Toft *et al*., 2010). Considering the errors on their
531 result, our results using EL chondrites match the BSE Th/U value, whereas models using
532 EH chondrites produce Th/U ratios significantly different (at 95% confidence) from the
533 estimated BSE value (Fig. 7). Although combinations of EL and EH chondrites are
534 possible scenarios for Earth's accretion (scenarios 3, 4, and 5, Table 4), EL chondrites
535 must represent the main portion of the mixture. This observation supports the notion that
536 EL rather than EH chondrites represent the dominant fraction of Earth's building blocks
537 (Boyet *et al*., 2018).
538
539 **4.2. Th/U ratio of the BSE and the oxygen content of Earth's core**
540 As discussed in section 3.2.3, our parameterizations of D_U and D_{Th} show that the
541 oxygen content of the Earth's core had a major impact on the fractionation of Th and U
542 during core segregation. Indeed, the most recent accretion models and high-pressure and
543 high-temperature studies suggest that Earth's core contains at least some amount of
544 oxygen (*e.g.*, Bouhifd and Jephcoat, 2011; Tsuno *et al*., 2013; Siebert *et al*., 2012; Badro
545 *et al*., 2014; Fischer *et al*., 2015; Rubie *et al*., 2015; and references therein). Existing
546 models propose a large range of plausible oxygen contents in the Earth's core. Based on
547 geochemical arguments, Allègre *et al*. (2001) concluded that the core contains 5.0 ± 0.5
548 wt% O, whereas Javoy *et al*. (2010) reported 2.55 ± 1.39 wt% O. By coupling
549 geochemical and geophysical constraints, Badro *et al*. (2014; 2015) concluded that the

core contains 2.7 to 5 wt% O. Fischer *et al*. (2015) estimated the oxygen content of the core by following similar accretion scenarios and found that the Earth's core contains 2.1–2.6 wt% O. Finally, to fit the present-day mantle concentrations of some moderately siderophile elements (Cr, V, and Mn), Siebert *et al*. (2013) suggested that the core should contain 2 to 5.5 wt% O. A general consensus of the literature can be found on a minimum content of oxygen in the core of 2 wt% O.

By tracing the evolution of the Th/U ratio of the BSE versus the oxygen content of the core (Fig. 8) using our parameterizations of D_U and D_{Th} (Eq. 4, Table 2), at 4.0 wt% O in the core, our modeled Th/U ratio of the BSE is beyond the 95% confidence level (2σ) of the BSE value. In this model, we equilibrate a CI-like chondritic composition with a proto-Earth (Barrat *et al*., 2012), simulating the last stages of core segregation when the most oxygen was incorporated into the metallic phase. For these calculations, we use the BSE Th/U value ($3.776^{+0.122}_{-0.075}$) given by Wipperfurth *et al*. (2018), which is in good agreement with several other studies (*e.g.*, Allègre *et al*., 1995; Kargel and Lewis, 1993). By combining the geophysical and geochemical constraints reported above with the added constraint of the Th/U ratio of the BSE, the core must contain 2 to 4 wt% O.

4.3 Impact of a late sulfide addition on U and Th partitioning

Another process that could have fractionated the Th/U ratio of the BSE is the late addition of sulfide (FeS) to the segregating core (*e.g.*, Wohlers and Wood, 2017). The S content of the Earth's core is about 2 wt% (*e.g.*, Allègre *et al*., 1995; Badro *et al*., 2014; Boujibar *et al*., 2014; Dreibus and Palme, 1996; Palme and O'Neill, 2003, and references therein), and different scenarios exist to explain how the Earth acquired sulfur during core

segregation. If S was added throughout Earth's accretion, we find that the U and Th contents of the core and the BSE would have barely been affected. If S was added exclusively in the last 10–20% of Earth's accretion (*e.g.* Wood and Halliday, 2005), our continuous core formation calculations show that the U and Th concentrations of the BSE would be lowered by 3%, whereas the variation of the Th/U ratio of the BSE would be negligible. Furthermore, our parameterizations (Eq. 4, Table 2) suggest that the late addition of sulfur-rich bodies would have increased the U and Th concentrations in the core by less than 6%. Thus, the late addition of sulfide (10–20%) to the Earth should not have drastically affected the U and Th contents of the BSE and the core, which contribute no more than 1 TW of the energy required to sustain the geodynamo. Finally, the addition of sulfide to the core, at any time during Earth's accretion, would not be observable based on the Th/U ratio of the BSE.

5. Conclusion

In the present study, we presented new metal – silicate partition coefficients of Th in a fully liquid environment. Combined with literature data from previous studies, we developed new parametrizations of the behavior of U and Th in the context of a magma ocean, that demonstrate the dependence of D_U and D_{Th} on the metallic melt composition and the temperature.

The new parameterizations are then used to better constrain the conditions of core formation and the composition of the core, in a multi-stage core growth models, by comparing the resulting $(Th/U)_{BSE}$ to the latest result by Wipperfurth *et al*. (2018). When considering building block mixing that reproduce the major isotopic and elementary

596 features of the BSE, the calculated concentrations (U_{BSE} = 11.42 ± 0.45 ppb and Th_{BSE} =
597 43.20 ± 1.73 ppb) best reproduce $(Th/U)_{BSE}$ when using reduced building blocks with an
598 EL chondrites type composition rather than EH. This support the idea that EL chondrites
599 (rather than EH) constitute a major part of Earth's reduced building blocks. In the
600 meantime, the contents U and Th in the Earth's core remain negligible, and cannot be
601 significantly affected by the addition of sulphur. Finally, we show that, in order to
602 reproduce the latest Th/U ratio of the BSE within its uncertainties (Wipperfurth *et al.*,
603 2018), the oxygen content of the Earth's core cannot exceed 4wt%.

Acknowledgments

We thank Denis Andrault, Nathalie Bolfan-Casanova, and Tahar Hammouda for fruitful discussions. We also thank xx for editorial handling. Official reviews by the associate editor as well as well as anonymous reviewers were helpful to improve the clarity of the paper.This project has received funding from the European Research Council (ERC) under the European Union's Horizon 2020 research and innovation programme (Grant Agreement No 682778 – ISOREE). The multi-anvil apparatus of Laboratoire Magmas et Volcans is financially supported by the CNRS (Instrument national de l'INSU). This work was also supported by the French Government Laboratory of Excellence Initiative N° ANR-10_LABX-006, the Région Auvergne, and the European Regional Development Fund. This is Laboratory of Excellence ClerVolc contribution N° 398.

617 **References**

618 Achterberg, E. van, Ryan, C.G., Jackson, S., and Griffin, W. (2001). Data reduction
619 software for LA-ICP-MS. In Laser-Ablation- ICPMS in the Earth Sciences,
620 Principles and Applications, pp. 239–243.

621 Allègre C., Poirier J.-P., Humler E. and Hofmann A. (1995) The chemical composition
622 of Earth. *Earth Planet. Sci. Lett.* **134**, 515–526.

623 Allègre, C., Manhès, G., and Lewin, É. (2001). Chemical composition of the Earth and
624 the volatility control on planetary genetics. Earth Planet. Sci. Lett. *185*, 49–69.

625 Andersen, M.B., Elliott, T., Freymuth, H., Sims, K.W.W., Niu, Y., and Kelley, K.A.
626 (2015). The terrestrial uranium isotope cycle. Nature 517, 356–359.

627 Andrault, D., Bolfan-Casanova, N., Nigro, G.L., Bouhifd, M.A., Garbarino, G., and
628 Mezouar, M. (2011). Solidus and liquidus profiles of chondritic mantle:
629 Implication for melting of the Earth across its history. Earth Planet. Sci. Lett. *304*,
630 251–259.

631 Badro, J., Brodholt, J.P., Piet, H., Siebert, J., and Ryerson, F.J. (2015). Core formation
632 and core composition from coupled geochemical and geophysical constraints.
633 Proc. Natl. Acad. Sci. *112*, 12310–12314.

634 Badro, J., Côté, A.S., and Brodholt, J.P. (2014) A seismologically consistent
635 compositional model of Earth's core. Proc. Natl. Acad. Sci. *111*, 7542–7545.

636 Barrat, J.A., Zanda, B., Jambon, A., and Bollinger, C. (2014). The lithophile trace
637 elements in enstatite chondrites. Geochimica et Cosmochimica Acta 128, 71–94.

638 Barrat, J.A., Zanda, B., Moynier, F., Bollinger, C., Liorzou, C., and Bayon, G. (2012).
639 Geochemistry of CI chondrites: Major and trace elements, and Cu and Zn
640 Isotopes. Geochimica et Cosmochimica Acta 83, 79–92.
641 Blanchard, I., Siebert, J., Borensztajn, S., and Badro, J. (2017). The solubility of heat-
642 producing elements in Earth's core. Geochem. Perspect. Lett. 1–5.
643 Blichert-Toft, J., Zanda, B., Ebel, D.S., and Albarède, F. (2010). The Solar System
644 primordial lead. Earth and Planetary Science Letters 300, 152–163.
645 Bouhifd, M.A., and Jephcoat, A.P. (2011). Convergence of Ni and Co metal–silicate
646 partition coefficients in the deep magma-ocean and coupled silicon–oxygen
647 solubility in iron melts at high pressures. Earth Planet. Sci. Lett. *307*, 341–348.
648 Bouhifd, M.A., Andrault, D., Bolfan-Casanova, N., Hammouda, T., and Devidal, J.L.
649 (2013). Metal–silicate partitioning of Pb and U: Effects of metal composition and
650 oxygen fugacity. Geochim. Cosmochim. Acta *114*, 13–28.
651 Bouhifd, M.A., Boyet, M., Cartier, C., Hammouda, T., Bolfan-Casanova, N., Devidal,
652 J.L., and Andrault, D. (2015). Superchondritic Sm/Nd ratio of the Earth: Impact
653 of Earth's core formation. Earth and Planetary Science Letters 413, 158–166.
654 Boujibar, A., Andrault, D., Bouhifd, M.A., Bolfan-Casanova, N., Devidal, J.L., Trcera,
655 N., (2014) Metal-silicate partitioning of sulfur, new experimental and
656 thermodynamical constraints on planetary accretion. Earth Planet. Sci. Lett. 391,
657 42–54.
658 Boujibar, A. *et al*. (2019) U, Th, and K partitioning between metal, silicate, and sulfide
659 and implications for Mercury's structure, volatile content, and radioactive heat
660 production. Am. Mineral. *104*, 1221-1237.

661 Boyet, M., Bouvier, A., Frossard, P., Hammouda, T., Garçon, M., Gannoun, A. (2018)
662 Enstatite chondrites EL3 as building blocks for the Earth: The debate over ^{146}Sm-
663 ^{142}Nd systematics. Earth Planet. Sci. Lett. *488*, 68–78.
664 Cartier, C., Hammouda, T., Boyet, M., Bouhifd, M.A., and Devidal, J.-L. (2014). Redox
665 control of the fractionation of niobium and tantalum during planetary accretion
666 and core formation. Nature Geoscience *7*, 573–576.
667 Chidester, B.A., Rahman, Z., Righter, K., and Campbell, A.J. (2017). Metal–silicate
668 partitioning of U: Implications for the heat budget of the core and evidence for
669 reduced U in the mantle. Geochim. Cosmochim. Acta *199*, 1–12.
670 Clesi, V., Bouhifd, M.A., Bolfan-Casanova, N., Manthilake, G., Fabbrizio, A., and
671 Andrault, D. (2016). Effect of H_2O on metal–silicate partitioning of Ni, Co, V, Cr,
672 Mn and Fe: Implications for the oxidation state of the Earth and Mars. Geochim.
673 Cosmochim. Acta *192*, 97–121.
674 Clesi, V., Bouhifd, M.A., Bolfan-Casanova, N., Manthilake, G., Schiavi, F., Raepsaet, C.,
675 Bureau, H., Khodja, H., and Andrault D. (2018) Low hydrogen contents in the
676 cores of terrestrial planets. Science Advances *4*, e1701876.
677 Corgne, A., Keshav, S., Wood, B.J., McDonough, W.F., and fei, Y. (2008) Metal-silicate
678 partitioning and constraints on core composition and oxygen fugacity during Earth
679 accretion. Geochim. Cosmochim. Acta *72*, 574–589.
680 Dauphas, N. (2017). The isotopic nature of the Earth's accreting material through time.
681 Nature *541*, 521–524.
682 Dauphas, N., Chen, J.H., Zhang, J., Papanastassiou, D.A., Davis, A.M., and Travaglio, C.
683 (2014). Calcium-48 isotopic anomalies in bulk chondrites and achondrites:

684 Evidence for a uniform isotopic reservoir in the inner protoplanetary disk. Earth
685 Planet. Sci. Lett. 407, 96–108.
686 Dauphas, N., and Pourmand, A. (2015). Thulium anomalies and rare earth element
687 patterns in meteorites and Earth: Nebular fractionation and the nugget effect.
688 Geochimica et Cosmochimica Acta 163, 234–261.
689 Deguen, R., Landeau, M., and Olson, P. (2014). Turbulent metal–silicate mixing,
690 fragmentation, and equilibration in magma oceans. Earth Planet. Sci. Lett. *391*,
691 274–287.
692 Dreibus, G., Palme, H., 1996. Cosmochemical constraints on the sulfur content of the
693 Earth's core. Geochim. Cosmochim. Acta *60*, 1125–1130.
694 Fischer, R.A., Nakajima, Y., Campbell, A.J., Frost, D.J., Harries, D., Langenhorst, F.,
695 Miyajima, N., Pollok, K., and Rubie, D.C. (2015). High pressure metal–silicate
696 partitioning of Ni, Co, V, Cr, Si, and O. Geochim. Cosmochim. Acta *167*, 177–
697 194.
698 Gagnon, J.E., Fryer, B.J., Samson, I.M., and Williams-Jones, A.E. (2008). Quantitative
699 analysis of silicate certified reference materials by LA-ICPMS with and without
700 an internal standard. J. Anal. At. Spectrom. *23*, 1529.
701 Gale, A., Dalton, C.A., Langmuir, C.H., Su, Y., and Schilling, J.-G. (2013). The mean
702 composition of ocean ridge basalts: MEAN MORB. Geochemistry, Geophysics,
703 Geosystems 14, 489–518.
704 Holzheid, A., Palme, H., and Chakraborty, S. (1997). The activities of NiO, CoO and FeO
705 in silicate melts. Chem. Geol. *139*, 21–38.

706 Javoy, M. (1995). The integral enstatite chondrite model of the Earth. Geophysical
707 Research Letters 22, 2219–2222.
708 Javoy, M., Kaminski, E., Guyot, F., Andrault, D., Sanloup, C., Moreira, M., Labrosse, S.,
709 Jambon, A., Agrinier, P., Davaille, A., et al. (2010). The chemical composition of
710 the Earth: Enstatite chondrite models. Earth and Planetary Science Letters 293,
711 259–268.
712 Jenner, F. E. & O'Neill, H. S. C. Analysis of 60 elements in 616 ocean floor basaltic
713 glasses. Geochem. Geophys. Geosyst. 13, 1–11 (2012).13. Q02005,
714 10.1029/2011GC004009.
715 Kargel, J.S., and Lewis, J.S. (1993). The composition and early evolution of earth. Icarus
716 *105*.
717 Kramers, J. D. & Tolstikhin, I. N. Two terrestrial lead isotope paradoxes, forward
718 transport modelling, core formation and the history of the continental crust. Chem.
719 Geol. 139, 75–110 (1997).
720 Lay, T., Hernlund, J., and Buffett, B.A. (2008). Core–mantle boundary heat flow. Nat.
721 Geosci. *1*, 25.
722 Li, J., and Agee, C.. (2001). The effect of pressure, temperature, oxygen fugacity and
723 composition on partitioning of nickel and cobalt between liquid Fe-Ni-S alloy and
724 liquid silicate: implications for the earth's core formation. Geochim. Cosmochim.
725 Acta *65*, 1821–1832.
726 Lyubetskaya, T., and Korenaga, J. (2007). Chemical composition of Earth's primitive
727 mantle and its variance. J. Geophys. Res. *112*.

728 Ma, Z. (2001). Thermodynamic description for concentrated metallic solutions using
729 interaction parameters. Metall. Mater. Trans. B *32*, 87–103.
730 Malavergne, V., Tarrida, M., Combes, R., Bureau, H., Jones, J., and Schwandt, C. (2007).
731 New high-pressure and high-temperature metal/silicate partitioning of U and Pb:
732 Implications for the cores of the Earth and Mars. Geochim. Cosmochim. Acta *71*,
733 2637–2655.
734 Mann, U., Frost, D.J., and Rubie, D.C. (2009). Evidence for high-pressure core-mantle
735 differentiation from the metal–silicate partitioning of lithophile and weakly-
736 siderophile elements. Geochimica et Cosmochimica Acta 73, 7360–7386.
737 McCubbin, F.M., Riner, M.A., Vander Kaaden, K.E., Burkemper, L.K. (2012) Is Mercury
738 a volatile-rich planet? Geophys. Res. Lett. *39*, L09202.
739 McDonough, W.F., and Sun, S, (1995). The composition of the Earth. Chemical Geology
740 120, 223–253.
741 Murrell, M.T., Burnett, D.S. (1986) Partitioning of K, U, and Th between sulfide and
742 silicate liquids: implications for radioactive heating of planetary cores. J.
743 Geophys. Res. 91, 8126-8136.
744 O'Neill, H.S.C., and Eggins, S.M. (2002). The effect of melt composition on trace
745 element partitioning: an experimental investigation of the activity coefficients of
746 FeO, NiO, CoO, MoO2 and MoO3 in silicate melts. Chem. Geol. *186*, 151–181.
747 Palme H., and O'Neill H. S. C. (2003) Cosmochemical estimates of mantle composition.
748 In *Treatise on Geochemistry, vol. 2* (eds. H. Holland and K. K. Turekian).
749 Elsevier, New York. pp. 1–38.

750 Palme, H., O'Neill, H.S.C. (2014) Cosmochemical estimates of mantle composition. In
751 Treatise on Geochemistry, vol. 2, edited by H. Holland and K. K. Turekian, pp. 1
752 – 38, Elsevier, New York.
753 Righter, K., and Drake, M.J. (2003). Partition coefficients at high pressure and
754 temperature. In The Mantle and Core, pp. 425–449.
755 Righter, K., Drake, M.J., and Yaxley, G., (1997) Prediction of siderophile element metal-
756 silicate partition coefficients to 20 GPa and 2800 °C: the effect of pressure,
757 temperature, oxygen fugacity, and silicate and metallic melt compositions. Phys.
758 Earth Planet. Int. *100*, 115-134.
759 Righter, K., Pando, K.M., Danielson, L., and Lee, C.-T. (2010). Partitioning of Mo, P and
760 other siderophile elements (Cu, Ga, Sn, Ni, Co, Cr, Mn, V, and W) between metal
761 and silicate melt as a function of temperature and silicate melt composition. Earth
762 Planet. Sci. Lett. *291*, 1–9.
763 Rubie, D.C., Jacobson, S.A., Morbidelli, A., O'Brien, D.P., Young, E.D., de Vries, J.,
764 Nimmo, F., Palme, H., and Frost, D.J. (2015). Accretion and differentiation of the
765 terrestrial planets with implications for the compositions of early-formed Solar
766 System bodies and accretion of water. Icarus 248, 89–108.
767 Rudge, J.F., Kleine, T., and Bourdon, B. (2010). Broad bounds on Earth's accretion and
768 core formation constrained by geochemical models. Nature Geoscience 3, 439–
769 443.
770 Siebert, J., Badro, J., Antonangeli, D., Ryerson, F.J., 2012. Metal–silicate partitioning of
771 Ni and Co in a deep magma ocean. Earth Planet. Sci. Lett. *321–322*, 189–197.

772 Siebert, J., Badro, J., Antonangeli, D., and Ryerson, F.J. (2013). Terrestrial Accretion
773 Under Oxidizing Conditions. Science 339, 1194–1197.
774 Siebert, J., Corgne, A., and Ryerson, F.J. (2011). Systematics of metal–silicate
775 partitioning for many siderophile elements applied to Earth's core formation.
776 Geochim. Cosmochim. Acta *75*, 1451–1489.
777 Taylor, S.R., Norman, M.D., 1990. Accretion of differentiated planetesimals to the Earth.
778 In: Newsom, H.E., Jones, J.H. (Eds.), Origin of the Earth. Oxford Univ. Press,
779 New York, pp. 29–43.
780 The Japan Society for the Promotion of Science and The Nineteenth Committee on
781 Steelmaking (1988) Part 2: Recommended values of activity and activity
782 coefficients, and interaction parameters of elements in iron alloys. In Steelmaking
783 Data Sourcebook. Gordon and Breach Science Publishers, New York. pp. 273–
784 297.
785 Toplis, M.J. (2004). The thermodynamics of iron and magnesium partitioning between
786 olivine and liquid: criteria for assessing and predicting equilibrium in natural and
787 experimental systems. Contrib. Mineral. Petrol. *149*, 22–39.
788 Tsuno, K., Frost, D.J., and Rubie, D.C. (2013). Simultaneous partitioning of silicon and
789 oxygen into the Earth's core during early Earth differentiation: simultaneous
790 partitioning of silicon and oxygen into earth's core. Geophysical Research Letters
791 40, 66–71.
792 Wade, J., and Wood, B.J. (2005). Core formation and the oxidation state of the Earth.
793 Earth Planet. Sci. Lett. *236*, 78–95.

794 Wasson, J.T., and Kallemeyn, G.W. (1988). Compositions of Chondrites. Philos. Trans.
795 R. Soc. Math. Phys. Eng. Sci. *325*, 535–544.
796 Wheeler, K.T., Walker, D., Fei, Y., Minarik, W.G., and McDonough, W.F. (2006).
797 Experimental partitioning of uranium between liquid iron sulfide and liquid
798 silicate: Implications for radioactivity in the Earth's core. Geochim. Cosmochim.
799 Acta *70*, 1537–1547.
800 Wipperfurth, S.A., Guo, M., Šrámek, O., and McDonough, W.F. (2018). Earth's
801 chondritic Th/U: Negligible fractionation during accretion, core formation, and
802 crust–mantle differentiation. Earth and Planetary Science Letters *498*, 196–202.
803 Wohlers, A., and Wood, B.J. (2015). A Mercury-like component of early Earth yields
804 uranium in the core and high mantle ^{142}Nd. Nature *520*, 337–340.
805 Wohlers, A., and Wood, B.J. (2017). Uranium, thorium and REE partitioning into sulfide
806 liquids: Implications for reduced S-rich bodies. Geochim. Cosmochim. Acta *205*,
807 226–244.
808 Wood, B.J., Halliday, A.N., 2005. Cooling of the Earth and core formation after giant
809 impact. Nature *437*, 1345–1348.
810 Wood, B.J., Walter, M.J., and Wade, J. (2006). Accretion of the Earth and segregation of
811 its core. Nature 441, 825–833.
812

Figure Captions

Figure 1. Backscattered electron image of sample #979 in its graphite capsule after polishing. This sample was prepared from a C1 chondrite model composition + FeNi as the starting material, and was recovered from 6 GPa and 2173 K.

Figure 2. Effect of the nature of the capsule (C or MgO) on U and Th partition coefficients. The experiments were performed at exactly the same conditions (~2073 K and 4 GPa or 2173 K and 6 GPa at IW –2), and we changed only the nature of the capsule. Runs 975 (4 GPa) and 1022 (6 GPa) were performed in graphite capsules, and runs 979 (4 GPa) and 986 (6 GPa) in MgO single-crystal capsules (Table 1).

Figure 3. Comparison between (a) U and (b) Th metal-silicate partition coefficients (D_U and D_{Th}, respectively) determined experimentally and predicted by multi-variable linear regressions (Eqs. 6 and 7). Solid and dotted lines represent the 1:1 correspondence and 1σ errors on our regression ($\sigma_U = 0.69$, $\sigma_{Th} = 0.85$), respectively. R^2 is 0.85 for U and 0.82 for Th. Data references are reported in Appendix B.

Figure 4. Evolution of D_{Th}/D_U as a function of pressure in S-free metal-silicate partitioning experiments of this study and Wohlers & Wood (2017).

Figure 5. Molten metal – silicate liquid partition coefficients as a function of oxygen fugacity. The experimental data are taken from Blanchard *et al*. (2017); Bouhifd *et al*. (2013); Chidester *et al*. (2017); Malavergne *et al*. (2007); Wheeler *et al*., (2006);

836 Wohlers & Wood (2017). These experimental data are corrected from the effect of *T* and
837 oxygen content of the metallic phase using the equations (6) and (7). In the present plot
838 we excluded data involving sulfide liquids, and only consider partitioning data between
839 silicate melt (with S content < 5 wt%) and Fe-rich alloys. The solid lines of slope -1 or -
840 0.5 represent uranium in valence 4+ or 2+, respectively.
841
842 **Figure 6.** Evolution of (a) U and (b) Th partition coefficients with the concentration
843 of S in the metallic phase for experiments performed below 10 GPa, between 2050 and
844 2350 K, and at around IW –2.
845
846 **Figure 7.** Compilation of Th/U ratios estimated for the BSE compared with the
847 results of this study. The grey line indicates the average BSE value of all studies shown
848 (Th/U = 3.70). All error bars are 1σ, except data from Wipperfurth et al. (2018) and this
849 study, for which error bars represent 2σ error propagations. Although our EL and EH
850 scenarios match the global geochemical models within 1σ uncertainties, only our EL
851 chondrite-based model is in agreement with the recent isotopic lead analysis of the BSE
852 Th/U value (Wipperfurth et al., 2018), suggesting EL chondrites as one of Earth's main
853 building blocks.
854
855 **Figure 8**. Evolution of the Th/U ratio of the BSE with the O content of the Earth's
856 core (black solid line). The calculations were made at 60 GPa and 3500 K. The grey solid
857 line represents the Th/U ratio observed in the BSE (Wipperfurth et al., 2018). The black
858 and grey dashed lines represent 2σ errors on the model and the observed BSE Th/U value,

859 respectively. The shaded area corresponds to unrealistic oxygen concentrations in the
860 metallic phase, based on previous studies (see text for references). The maximum value
861 of 3.95 wt% O varies little with modification of the final parameters of the model such as
862 *P*, *T*, and the chemical composition of the building blocks.

Figure 1.

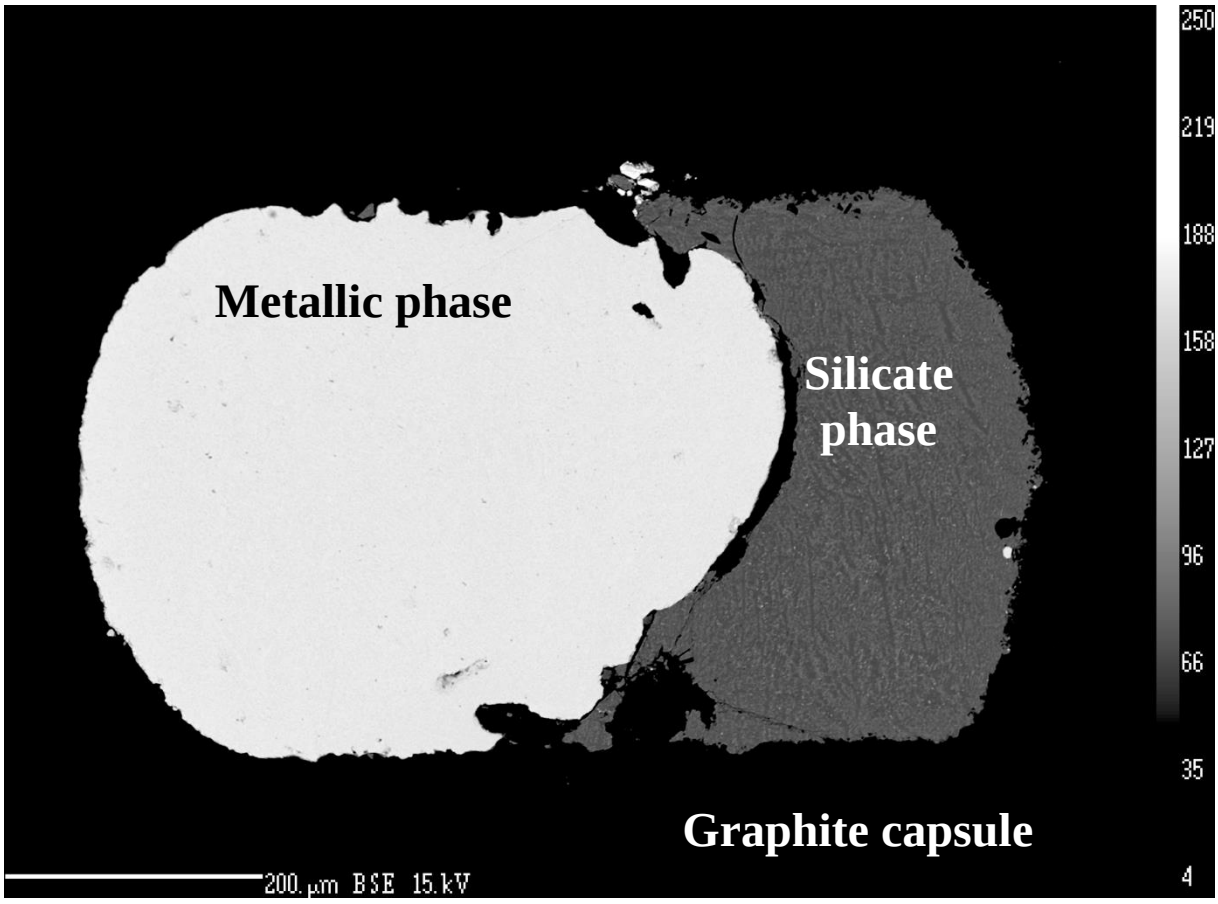
Metallic phase
Silicate phase
Graphite capsule
200.µm BSE 15.kV
250
219
188
158
127
96
66
35
4

Figure 2.

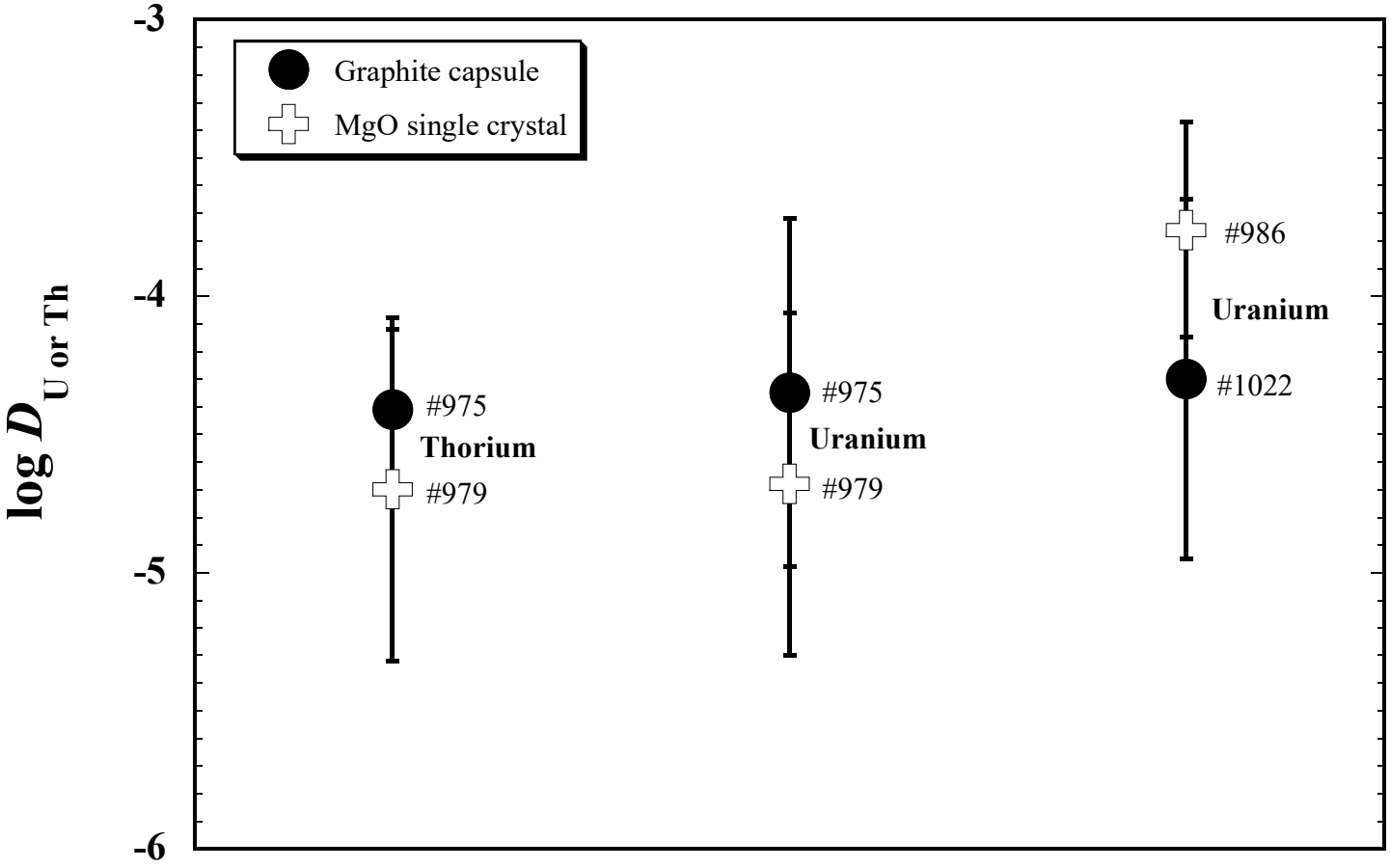
-3
-4
-5
-6
log $D_{U\ or\ Th}$
Graphite capsule
MgO single crystal
#975
Thorium
#979
#975
Uranium
#979
#986
Uranium
#1022

Figure 3a.

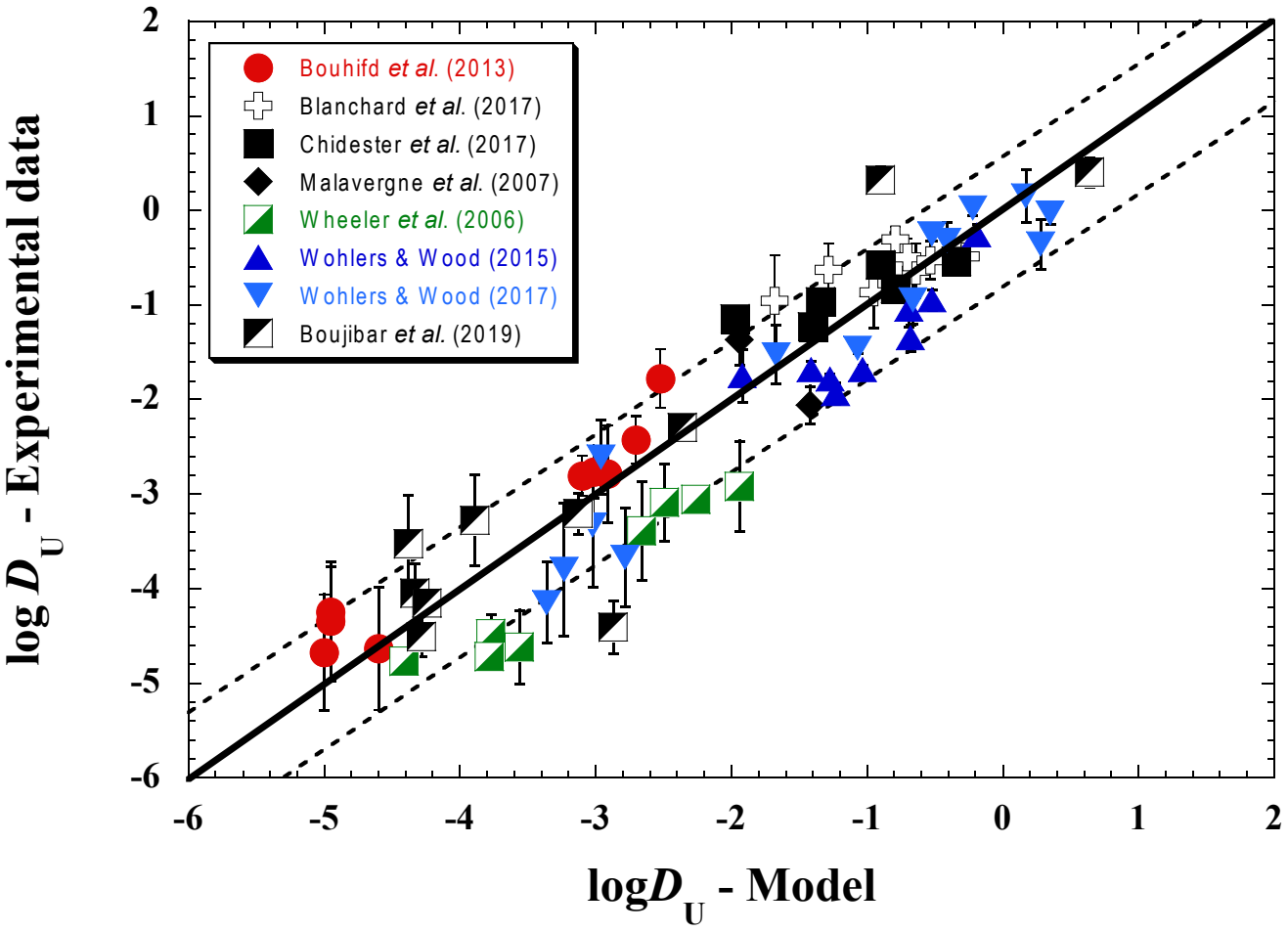

Figure 3b.

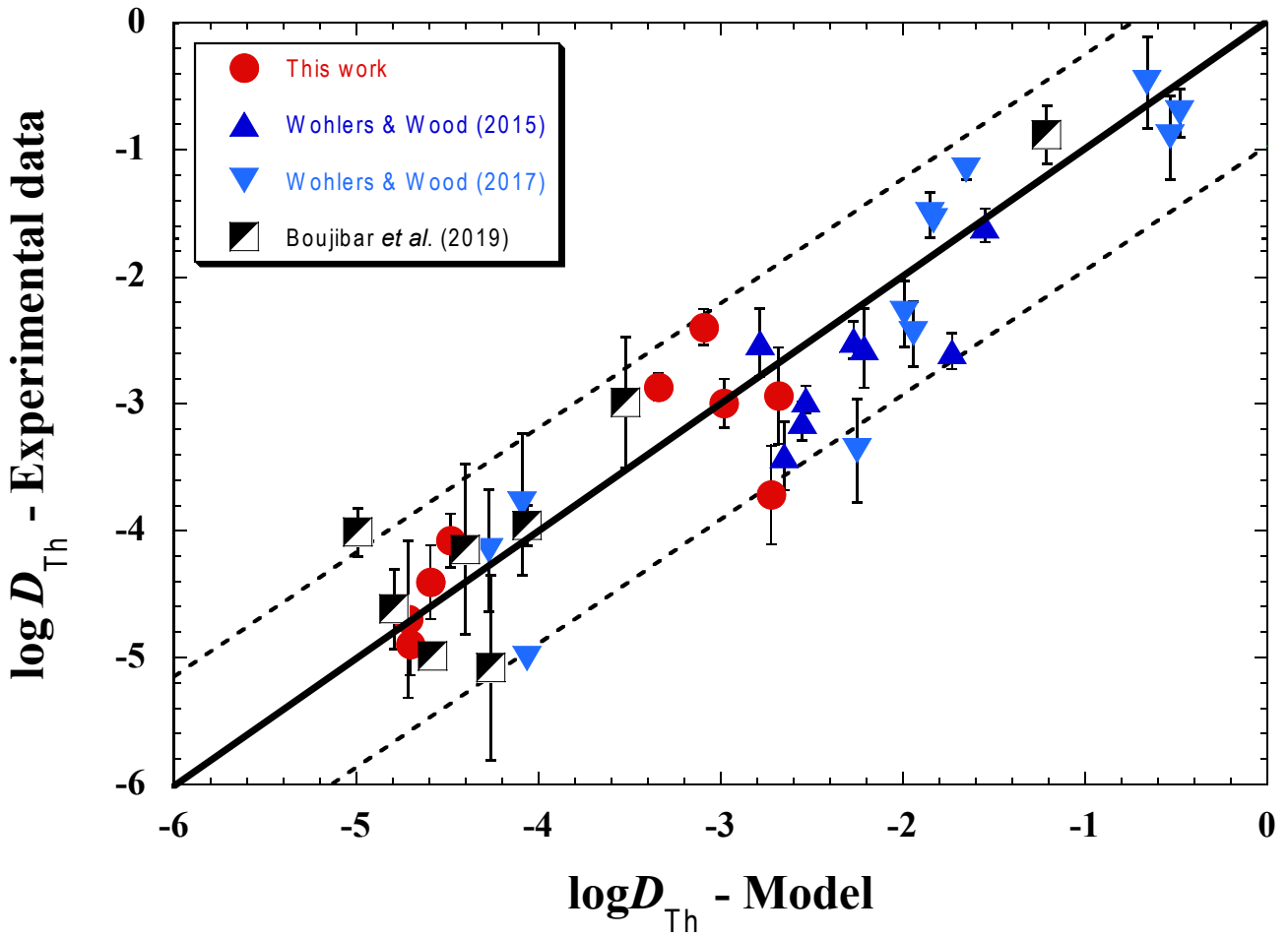

Figure 4.

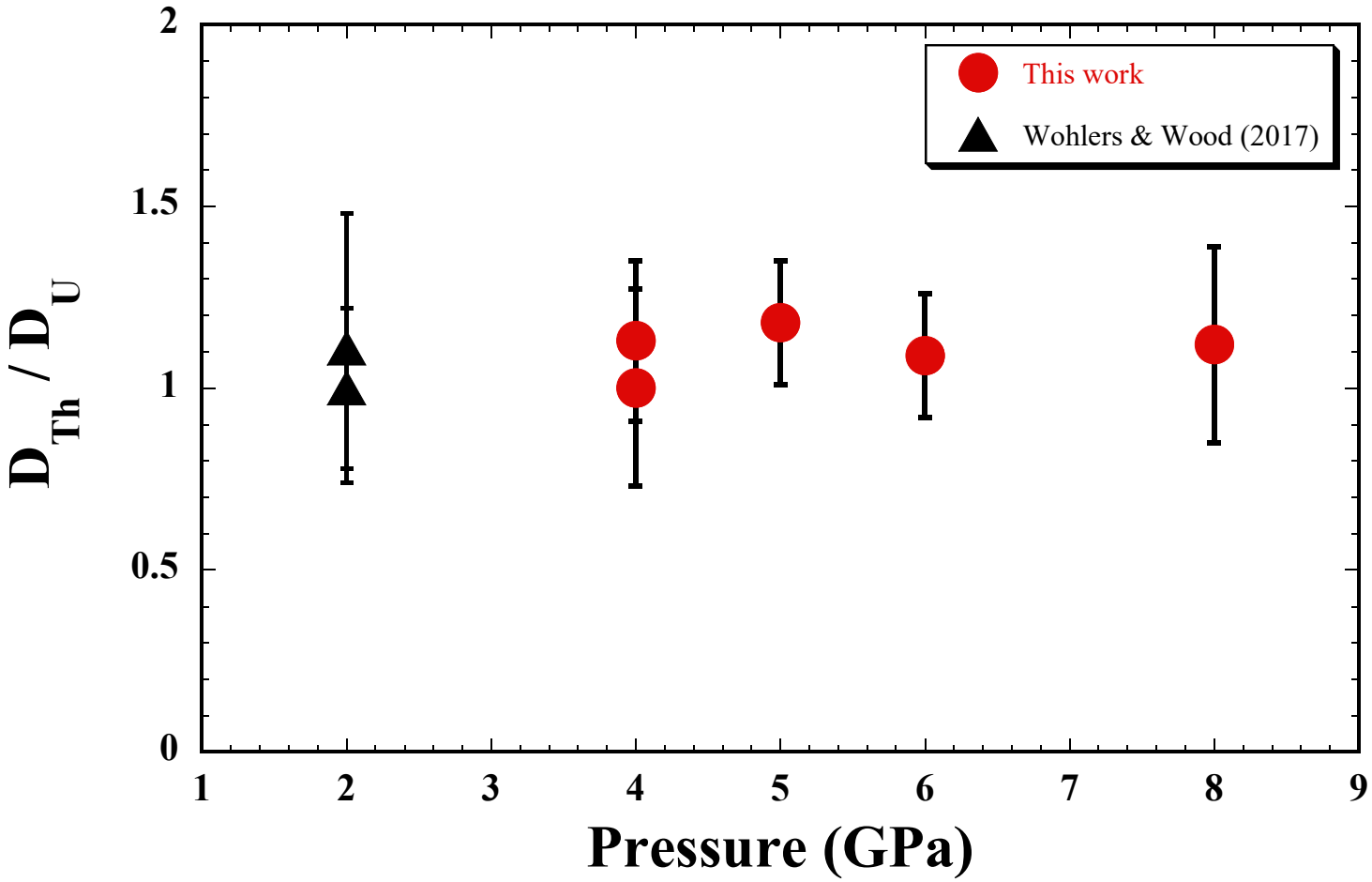
This work
Wohlers & Wood (2017)
D_{Th} / D_U
Pressure (GPa)
0
0.5
1
1.5
2
1
2
3
4
5
6
7
8
9

Figure 5.

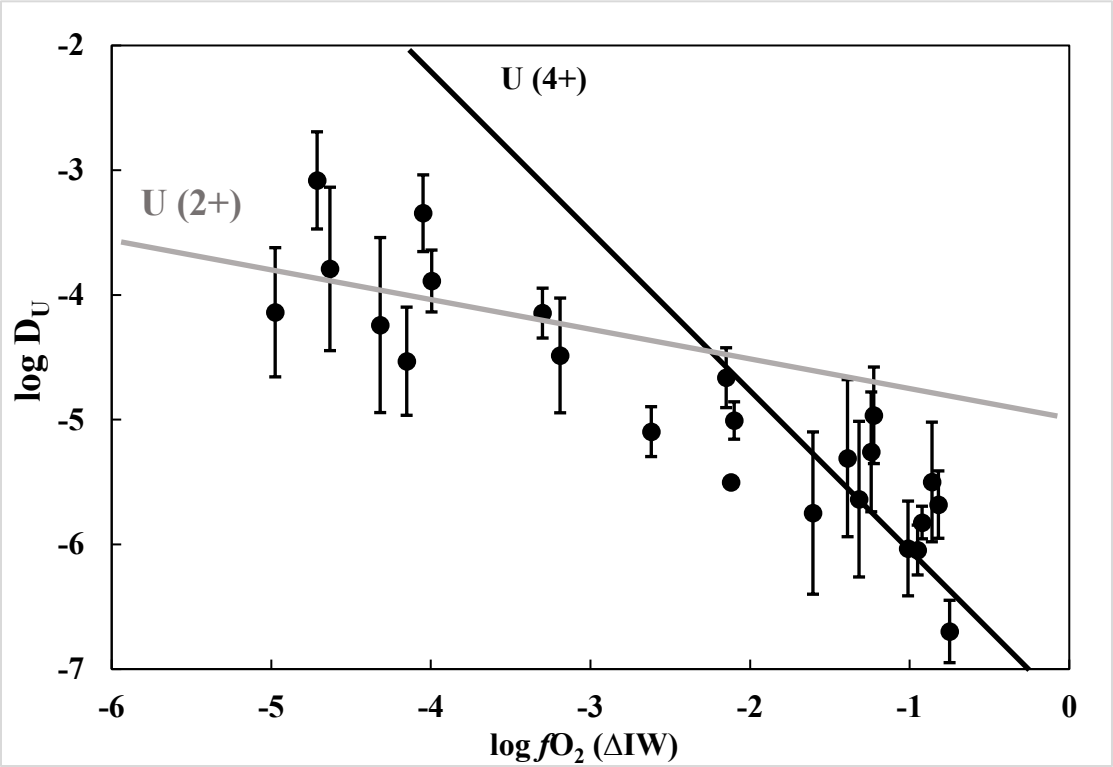

Figure 6a.

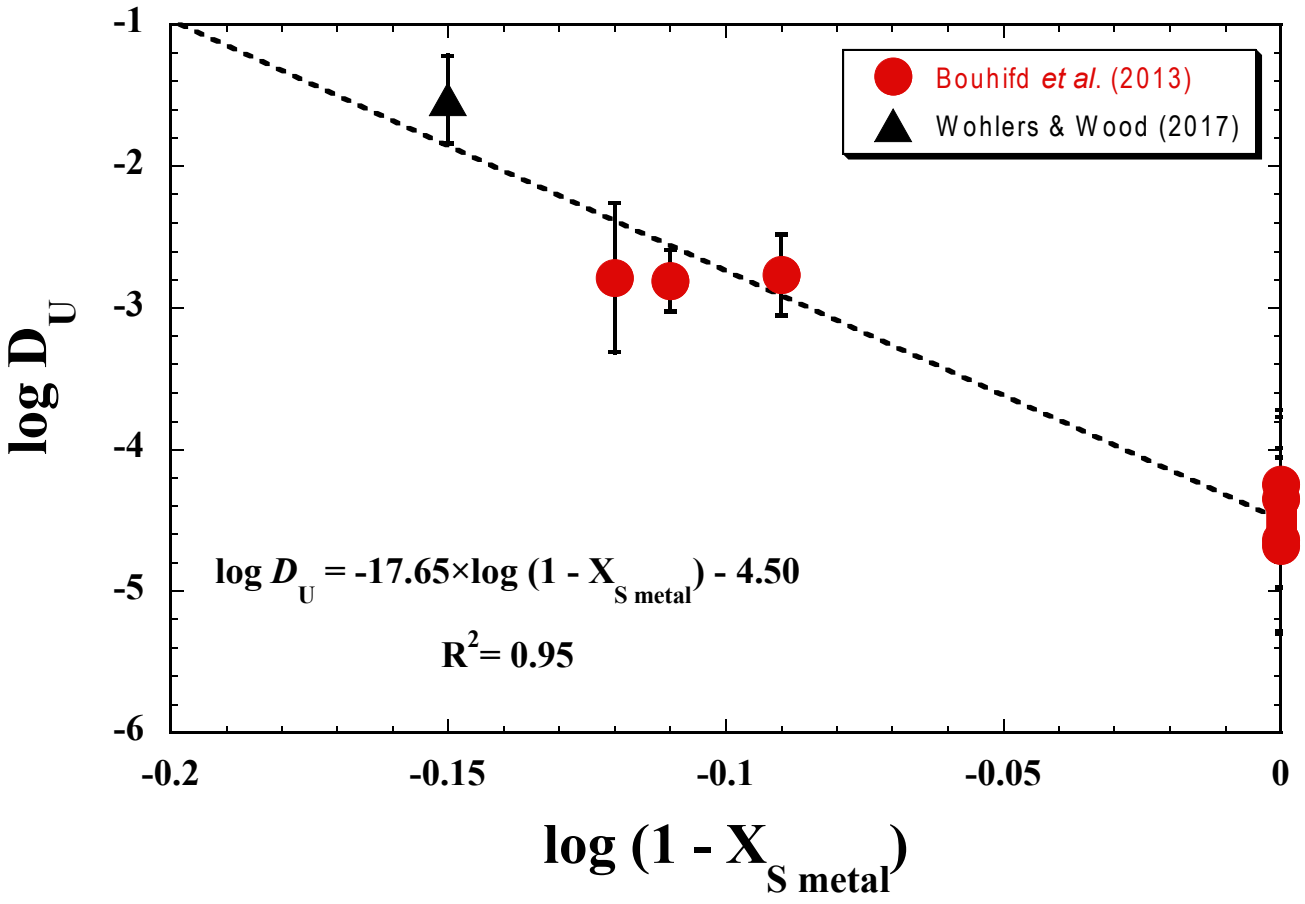

Figure 6b.

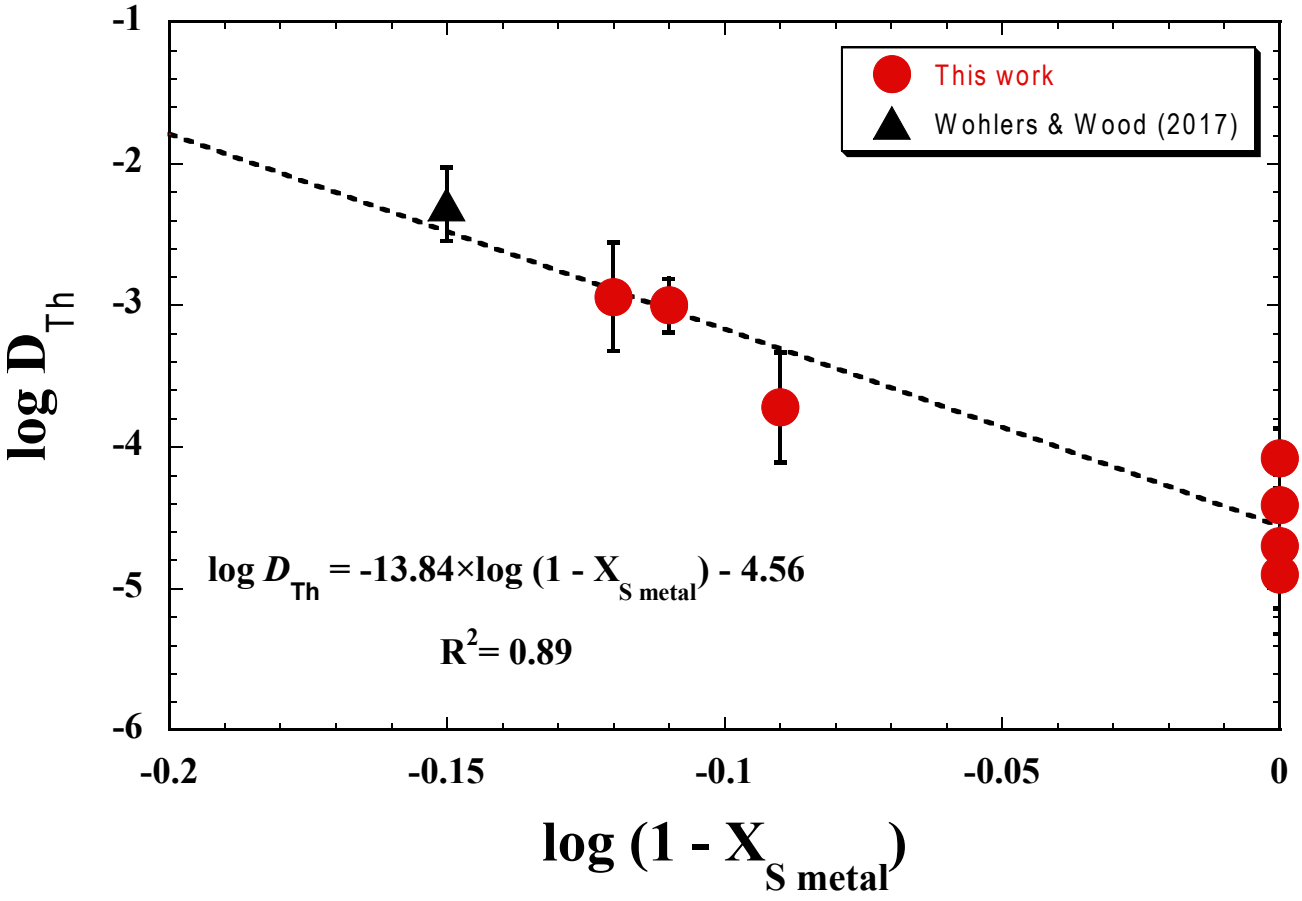

Figure 7.

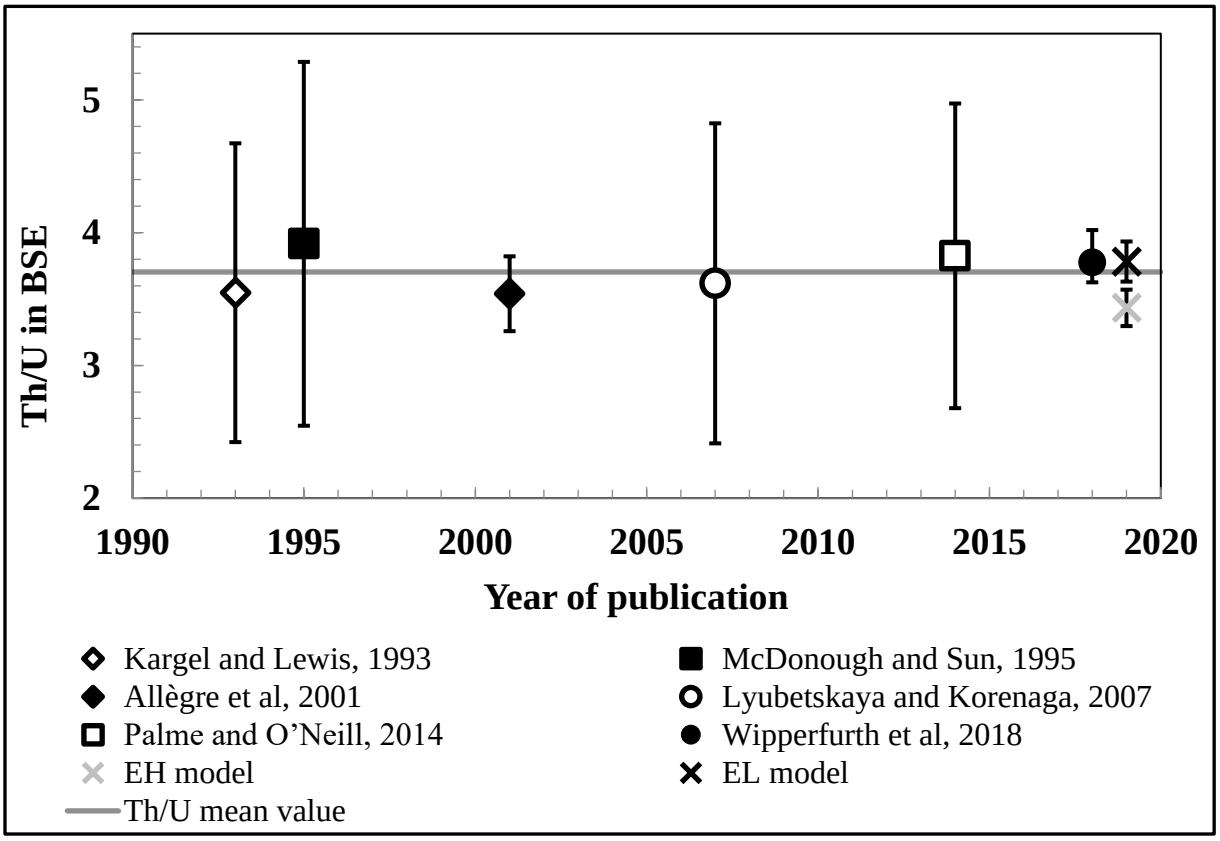
Th/U in BSE
5
4
3
2
1990
1995
2000
2005
2010
2015
2020
Year of publication
Kargel and Lewis, 1993
Allègre et al, 2001
Palme and O'Neill, 2014
EH model
Th/U mean value
McDonough and Sun, 1995
Lyubetskaya and Korenaga, 2007
Wipperfurth et al, 2018
EL model

Figure 8.

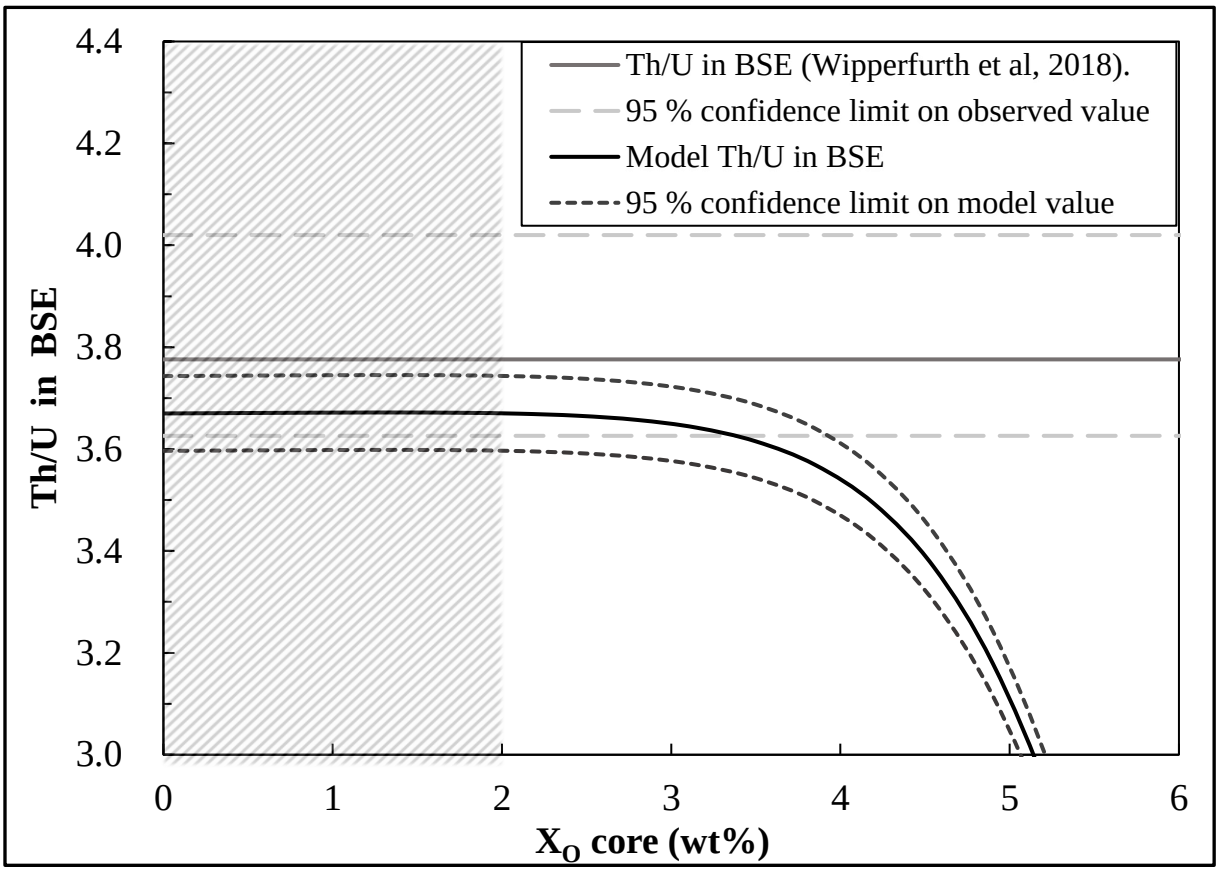
Th/U in BSE (Wipperfurth et al, 2018).
95 % confidence limit on observed value
Model Th/U in BSE
95 % confidence limit on model value
Th/U in BSE
4.4
4.2
4.0
3.8
3.6
3.4
3.2
3.0
0
1
2
3
4
5
6
X_O core (wt%)

Table 1. Experimental conditions (P, T, f_{O_2}) and metal - silicate partitioning coefficients of U and Th for the different samples.

Sample	**Capsule**	**P** (Gpa)	**T** (K)	**log *f*O₂ (ΔIW)**	**D_U***	**D_{Th}**
#969	Graphite	4	2128	-1.43	5.65×10^{-5}	3.86×10^{-5}
#975	Graphite	4	2073	-1.56	4.51×10^{-5}	1.26×10^{-5}
#1026	Graphite	5	2273	-0.82	1.64×10^{-3}	1.14×10^{-3}
#1027	Graphite	5	2273	-4.42	3.73×10^{-3}	1.34×10^{-3}
#1022	Graphite	6	2173	-1.74	2.30×10^{-5}	
#979	MgO	4	2075	-1.70	2.07×10^{-5}	2.02×10^{-5}
#986	MgO	6	2173	-1.64	1.76×10^{-4}	8.22×10^{-5}
#1021	MgO	6	2173	-1.44	1.54×10^{-3}	9.92×10^{-5}
#1028	MgO	8	2373	-1.45	1.71×10^{-3}	1.89×10^{-4}
#1029	MgO	8	2373	-4.67	1.64×10^{-2}	4.00×10^{-3}

***** *The partition coefficient values of U are taken from Bouhifd et al., 2013.*

Table 2. Results of the multi-variable linear regression based on Equation 4 using our experimental data together with those listed in Appendix B.

Elements	*Nº.*	R^2	*a*	*b*	*d*	*f*	*cst*
U	**74**	0.85	-0.72 ± 0.07	-8346 ± 1103	-15.33 ± 1.13	-51.55 ± 7.86	-1.53 ± 0.52
Th	**44**	0.82	-0.96 ± 0.10	-9967 ± 2618	-13.76 ± 1.40	-137.82 ± 26.63	0.77 ± 1.12

N^o.: number of experiments; R^2: correlation coefficient.

Table 3. U and Th abundances (in ppb) for CI and EC chondrites used in this work. Only samples which fall where observed have been selected here, taken from the most recent published trace element measurements on chondrites. The *n* value represents the number of samples the U and Th concentration are based on.

	n	**U**	**1σ**	**Th**	**1σ**	**Th/U**	**1σ**	***references***
CI chondrites	*7*	7.72	0.23	28.30	1.42	3.66	0.11	*Barrat et al, 2012*
EL chondrites	*8*	6.60	1.00	28.70	3.11	4.39	0.52	*Barrat et al, 2014; Dauphas and Pourmand, 2015*
EH chondrites	*7*	8.33	0.69	26.95	1.51	3.24	0.17	

Table 4. Different scenarios of Earth's accretion involving reducing chondrites (EH or EL type) and more oxidized ones (CI, CO, CV or CM) in various proportions. CI, EH and EL concentrations are presented in Table 3. Other chondrite compositions are taken from Wasson and Kallemeyn (1988), but scenarios 5,6 and 7 show that recent CI chondrites U and Th concentrations can be used as a proxy for carbonaceous chondrites. The uncertainties presented here are all 2$\boldsymbol{\sigma}$. Nb/Ta and Ni/Co ratios of the resulting BSE as well as the Si and O content of the associated core are calculated for each scenario. Each scenario presented here reproduce, within 2 $\boldsymbol{\sigma}$ uncertainties, the Nb/Ta and Ni/Co of the BSE, presented for comparison in the last row of this table. Nb/Ta, Ni/Co and Th/U of the BSE, are taken from Münker et al. (2003), Lyubetskaya and Korenaga (2007) and Wipperfurth et al. (2018), respectively. Scenarios 9 and 10 are building block mixing proposed by Dauphas et al. (2014) and Dauphas, (2017), respectively. For these scenarios, since no precision is given considering the EC type used in these scenarios, we used the average of the EH and EL values given in Table 3, CI chondrites were considered as representative of carbonaceous chondrites (CC) chondrites and ordinary chondrites (OC) concentrations is an average of L LL and H chondrites concentration taken from Wasson and Kallemeyn (1988).

Scenario	**Reduced material %**		**Oxidized material %**		**BSE (ppb)**					**Core (ppb)**	
					Nb/Ta	**Ni/Co**	**U**	**Th**	**Th/U**	**U (ppm)**	**Th (ppm)**
1	EH	80	CI	20	13.75 ±*0.55*	19.1 ±*0.80*	11.77 ±*0.45*	40.42 ±*1.62*	3.43 ±*0.13*	1.28 ±*0.05*	4.80 ±*0.20*
2	EL	80	CI	20	14.68 ±*0.59*	18.7 ±*0.76*	11.42 ±*0.48*	43.20 ±*1.73*	3.78 ±*0.15*	1.24 ±*0.07*	5.22 ±*0.21*
3	EH-EL	40-40	CI	20	13.76 ±*0.56*	19.1 ±*0.78*	11.61 ±*0.46*	41.88 ±*1.67*	3.60 ±*0.14*	1.24 ±*0.05*	4.82 ±*0.20*
4	EH-EL	20-60	CI	20	14.03 ±*0.57*	19.1 ±*0.77*	11.51 ±*0.46*	42.52 ±*1.70*	3.69 ±*0.15*	1.25 ±*0.06*	5.05 ±*0.20*
5	EH-EL	60-20	CI	20	13.75 ±*0.56*	19.1 ±*0.79*	11.68 ±*0.47*	41.16 ±*1.64*	3.52 ±*0.14*	1.28 ±*0.05*	4.83 ±*0.20*
6	EL	80	CM	20	13.08 ±*0.60*	19.45 ±*0.81*	11.49 ±*0.46*	43.20 ±*2.20*	3.76 ±*0.25*	1.24 ±*0.12*	5.23 ±*0.42*
7	EL	80	CO	20	14.46 ±*0.55*	19.23 ±*0.84*	11.46 ±*0.63*	42.40 ±*2.06*	3.70 ±*0.23*	1.24 ±*0.11*	5.23 ±*0.41*
8	EL	80	CV	20	13.88 ±*0.54*	19.27 ±*0.82*	11.40 ±*0.72*	42.18 ±*2.51*	3.70 ±*0.30*	1.25 ±*0.16*	5.24 ±*0.56*
9	EC	91	OC-CC	7-2	11.28 ±*0.66*	18.75 ±*0.89*	11.39 ±*0.85*	42.82 ±*2.02*	3.76 ±*0.32*	1.25 ±*0.13*	5.29 ±*0.51*
10	EC	71	OC-CO	5-24	12.23 ±*0.61*	19.73 ±*0.88*	11.80 ±*0.83*	43.66 ±*2.06*	3.70 ±*0.32*	1.20 ±*0.13*	5.15 ±*0.50*
BSE					**14.00 ±*0.60***	**18.90 ±*0.32***			**3.78 ±*0.24***		

Appendix A. Chemical analysis of all the run products.

Table A1. Chemical analysis of the run products using graphite capsules.

P (GPa)[1]	4	4	5	5	6
T (K)[2]	2128	2073	2273	2273	2173
Run	969	975	1026	1027	1022
Silicate					
EPMA (wt%)					
SiO_2	48.93±0.57	48.20±0.43	43.00±0.89	54.05±0.39	50.37±0.42
Al_2O_3	4.33±0.31	3.72±0.22	3.59±0.42	3.83±0.10	2.60±0.12
FeO	8.44±0.13	7.54±0.17	13.83±0.63	0.32±0.04	7.50±0.45
MgO	33.29±0.77	36.39±0.55	33.93±0.82	35.76±0.49	34.86±0.53
CaO	2.87±0.11	2.77±0.13	2.60±0.21	3.05±0.05	2.88±0.12
K_2O	0.47±0.02	0.44±0.03	2.25±0.22	2.47±0.03	0.30±0.03
NiO	0.13±0.01	0.19±0.02	0.14±0.02	n.d.	0.13±0.02
PbO	0.16±0.01	0.14±0.01	n.d.	n.d.	0.09±0.01
UO_2	0.54±0.03	0.52±0.03	0.21±0.02	0.17±0.01	0.48±0.03
Total	99.16	99.91	99.56	100.13	99.21
LA-ICP-MS (ppm)					
U	3896±100	3769±156	905±108	1126±22	4353±220
Th	3881±72	3957±163	879±71	1100±12	4120±140
Metal					
EPMA (wt%)					
Fe	58.73±0.59	61.03±1.10	54.01±1.20	83.30±0.32	74.61±0.68
Ni	36.55±0.76	35.42±0.99	19.60±1.10	0.07±0.04	20.25±0.69
S	--	--	23.28±0.82	--	--
Si	--	--	--	15.76±0.65	--
Pb	0.73±0.10	0.33±0.14	0.11±0.01	n.d.	0.10±0.02
[3]O	0.03±0.01	0.05±0.04	0.75±0.13	0.16±0.02	0.03±0.02
Total	96.32	97.06	97.86	99.51	95.20
LA-ICP-MS (ppm)					
U	0.22±0.10	0.17±0.10	1.48±0.60	4.2±0.96	0.10±0.06
Th	0.15±0.04	0.05±0.01	1.00±0.30	1.47±0.15	n.d.
[3]$\log f_{O2}$ (ΔIW)	-1.81	-1.95	-1.25	-4.95	-2.07
[4]$\log f_{O2}$ (ΔIW)	-1.43	-1.56	-0.82	-4.42	-1.74
D_U	5.6×10^{-5}	4.5×10^{-5}	1.6×10^{-3}	3.7×10^{-3}	2.3×10^{-5}
	$\pm 2.7 \times 10^{-5}$	$\pm 2.8 \times 10^{-5}$	$\pm 0.8 \times 10^{-3}$	$\pm 0.9 \times 10^{-3}$	$\pm 1.5 \times 10^{-5}$
D_{Th}	3.9×10^{-5}	1.3×10^{-5}	1.1×10^{-3}	1.3×10^{-3}	
	$\pm 1.1 \times 10^{-5}$	$\pm 0.3 \times 10^{-5}$	$\pm 0.4 \times 10^{-3}$	$\pm 0.15 \times 10^{-3}$	

Table A2. Chemical analyses of run products using MgO-single crystal capsules (wt%).

P (GPa)[1]	4	6	6	8	8
T (K)[2]	2075	2173	2173	2373	2373
Run	979	986	1021	1028	[4]1029
Silicate					
EPMA (wt%)					
SiO_2	48.20±0.85	47.00±0.76	49.75±1.20	47.84±0.82	47.41±0.71
Al_2O_3	4.14±0.46	5.80±0.42	2.60±0.25	4.06±0.39	4.31±0.24
FeO	8.86±0.55	8.00±0.51	9.50±0.62	9.12±0.53	0.31±0.02
MgO	35.41±0.77	34.45±0.85	33.86±0.85	34.41±0.78	37.73±0.95
CaO	2.57±0.38	2.55±0.32	1.90±0.21	2.45±0.24	2.55±0.15
K_2O	0.35±0.02	0.37±0.03	0.18±0.04	1.25±0.46	3.15±0.17
NiO	0.14±0.01	0.14±0.01	0.13±0.01	0.10±0.01	n.d.
PbO	0.05±0.02	n.d.	n.d.	n.d.	0.10±0.01
UO_2	0.36±0.05	0.35±0.05	0.11±0.01	0.10±0.02	0.28±0.02
Total	100.08	98.66	98.03	99.33	95.84
LA-ICPMS (ppm)					
U	3858±478	3300±424	846±76	850±130	859±51
Th	3969±491	3162±67	1008±95	899±190	851±41
Metal					
EPMA (wt%)					
Fe	66.91±0.54	56.11±0.90	61.39±1.53	60.34±0.9	84.64±0.59
Ni	30.02±0.22	40.52±0.58	17.97±0.81	18.24±0.57	0.26±0.07
S	--	--	20.03±0.82	19.69±0.33	--
Si	--	--	--	--	13.81±0.31
Pb	0.38±0.06	0.23±0.03	0.12±0.01	0.19±0.02	0.27±0.10
[3]O	0.05±0.02	0.06±0.02	0.33±0.04	0.42±0.04	0.05±0.03
Total	97.57	97.12	99.94	98.9	99.24
LA-ICPMS (ppm)					
U	0.08±0.04	0.58±0.15	1.30±0.16	1.45±0.36	14.1±3.5
Th	0.08±0.04	0.26±0.05	0.10±0.01	0.17±0.05	3.4±0.3
[5]log f_{O2} (ΔIW)	-2.05	-1.99	-1.76	-1.80	-5.02
[6]log f_{O2} (ΔIW)	-1.70	-1.64	-1.44	-1.45	-4.67
D_U	2.1×10^{-5}	1.8×10^{-4}	1.5×10^{-3}	1.7×10^{-3}	1.6×10^{-2}
	$\pm 1.3 \times 10^{-5}$	$\pm 0.7 \times 10^{-4}$	$\pm 0.3 \times 10^{-3}$	$\pm 0.7 \times 10^{-3}$	$\pm 0.5 \times 10^{-2}$
D_{Th}	6.05×10^{-5}	8.2×10^{-5}	9.9×10^{-5}	1.9×10^{-4}	4.0×10^{-3}
	$\pm 2.00 \times 10^{-5}$	$\pm 1.8 \times 10^{-5}$	$\pm 1.9 \times 10^{-5}$	$\pm 1.0 \times 10^{-4}$	$\pm 0.5 \times 10^{-3}$

n.d. not analysed.

[1]Pressure uncertainties are estimated to be ± 0.5 GPa of the reported values.

[2]Temperature uncertainties are within ± 100 K.

[3]Oxygene concentration in metal is the result of microprobe analysis in samples subtracted of the concentration analyzed in pure Fe sample Nist665 ($Xo_{Nist665}$=0.21±0.01 wt%).

[4]For the run #1029, total of about 1.5 wt% of trace elements in the silicate are not reported.

[5]Oxygen fugacities relative to Iron-Wüstite buffer assuming that the activities of Fe and FeO were equal to their mole fraction.

[6]Oxygen fugacities relative to Iron-Wüstite buffer assuming that γ_{FeO} = 1.5. and γ_{Fe} is calculated using the formula of Ma, 2001.

Appendix B. Compilation of the experimental data used to derive the coefficients of Equation (4) for U and Th. The uncertainties on the reported data can be found in the original papers.

D_U	D_{Th}	$log(f_{O2})$ (ΔIW)	P (Gpa)	T (K)	$X_{S\ metal}$ (wt.%)	$X_{c\ metal}$ (wt.%)	$X_{Si\ metal}$ (wt.%)	$X_{O\ metal}$ (wt.%)
This work *(*Data presented in Bouhifd et al, 2013)*								
$^{*}2.30\times10^{-5}$		-1.74	6	2173	0.00	4.8	0.00	0.03
$^{*}4.51\times10^{-5}$	1.26×10^{-5}	-1.56	4	2073	0.00	2.94	0.00	0.05
$^{*}2.07\times10^{-5}$	2.02×10^{-5}	-1.70	4	2075	0.00	0.00	0.00	0.05
$^{*}1.64\times10^{-3}$	4.00×10^{-3}	-0.82	5	2273	23.28	2.14	0.00	0.75
$^{*}5.65\times10^{-5}$	3.86×10^{-5}	-1.43	4	2128	0.00	3.68	0.00	0.03
$^{*}1.76\times10^{-4}$	8.22×10^{-5}	-1.64	6	2173	0.00	0.00	0.00	0.06
$^{*}1.64\times10^{-2}$	1.14×10^{-3}	-4.67	8	2373	0.00	0.00	13.81	0.05
$^{*}1.71\times10^{-3}$	1.89×10^{-4}	-1.45	8	2373	19.69	0.00	0.00	0.42
$^{*}3.73\times10^{-3}$	1.34×10^{-3}	-4.42	5	2273	0.00	0.49	15.76	0.16
$^{*}1.54\times10^{-3}$	9.92×10^{-5}	-1.44	6	2173	20.03	0.00	0.00	0.33
Malavergne et al., 2007								
4.70×10^{-2}		-4.80	20	2673	33.30	0.00	1.50	0.00
4.30×10^{-2}		-5.40	5	2173	0.00	0.00	9.10	0.00
8.65×10^{-3}		-4.80	20	2673	2.30	2.10	26.60	0.00
Wheeler et al., 2006								
3.30×10^{-5}		-2.06	2	2373	2.40	0.00	0.00	0.00
1.70×10^{-5}		-2.02	2	2123	0.10	0.00	0.00	0.00
4.10×10^{-4}		-2.23	2	2123	21.40	0.00	0.00	0.00
2.40×10^{-5}		-2.31	3	2123	9.30	0.00	0.00	0.00
1.20×10^{-3}		-1.92	10	2273	28.80	0.00	0.00	0.00
8.70×10^{-4}		-1.80	10	2123	29.30	0.00	0.00	0.00
1.90×10^{-5}		-1.98	10	2223	6.80	0.00	0.00	0.00
8.20×10^{-4}		-1.83	10	2073	27.70	0.00	0.00	0.00

Wohlers and Wood, 2015

1.14×10^{-2}	3.88×10^{-4}	-2.57	2	1673	36.85	0.00	0.00	0.92
2.05×10^{-2}	7.24×10^{-4}	-3.42	2	1673	36.00	0.00	0.00	0.36
1.13×10^{-1}	3.15×10^{-3}	-4.09	2	1673	36.86	0.00	0.00	0.21
$1.53\times10^{+1}$	7.29×10^{-1}	-4.19	2	1673	35.63	0.00	0.00	0.20
1.79×10^{-2}	3.69×10^{-3}	-1.16	2	1673	33.24	0.00	0.00	3.06
4.45×10^{-2}	2.55×10^{-3}	-2.99	2	1923	36.68	0.00	0.00	0.37
5.52×10^{-1}	2.52×10^{-2}	-4.03	2	1923	35.55	0.00	0.00	0.21
5.83	2.58×10^{-1}	-4.20	2	1923	32.92	0.00	0.00	0.21
7.05	2.44×10^{-1}	-4.24	2	1923	33.82	0.00	0.00	0.16
8.86×10^{-2}	2.74×10^{-3}	-4.03	2	1773	33.89	0.00	0.00	0.24
3.17	1.28×10^{-1}	-4.39	2	1773	32.18	0.00	0.00	0.51
1.64×10^{-2}	1.07×10^{-3}	-1.81	2	1773	35.46	0.00	0.00	1.98
2.03×10^{-2}	3.03×10^{-3}	-1.45	2	1773	33.40	0.00	0.00	3.18

Wohlers and Wood, 2017

3.46×10^{-2}	4.26×10^{-4}	-4.07	2	1908	29.31	2.45	0.00	0.15
1.13×10^{-1}	3.57×10^{-3}	-4.15	2	1908	32.17	2.44	0.02	0.07
5.67×10^{-1}	3.10×10^{-2}	-4.20	2	1908	32.83	2.92	0.02	0.14
4.83×10^{-1}	2.76×10^{-2}	-4.21	2	1908	32.56	4.28	0.02	0.39
1.04	6.97×10^{-2}	-4.27	2	1908	34.23	3.90	0.01	0.18
4.42×10^{-1}	1.25×10^{-1}	-3.93	2	2373	35.49	2.51	0.01	0.01
3.57×10^{-3}	1.95×10^{-1}	-3.98	2	2373	35.73	2.87	0.01	0.05
1.42	3.41×10^{-1}	-3.83	2	2373	34.50	2.96	0.80	0.47
4.63×10^{-2}	5.14×10^{-3}	-0.78	2	2373	28.94	1.62	0.08	3.91
7.12×10^{-5}	6.92×10^{-5}	-4.62	2	1923	0.00	0.00	1.79	0.00
1.11×10^{-4}	4.47×10^{-6}	-4.96	2	1923	0.00	0.00	3.42	0.00
2.02×10^{-4}	9.82×10^{-6}	-5.41	2	1923	0.00	0.00	8.25	0.00
2.11×10^{-4}	8.31×10^{-5}	-5.66	2	1923	0.00	0.00	10.94	0.00
3.04×10^{-4}	7.69×10^{-5}	-4.60	2	1923	0.00	4.43	2.61	0.03
1.59×10^{-4}	7.84×10^{-4}	-4.97	2	1923	0.00	4.43	6.08	0.09

8.41×10^{-4}	8.53×10^{-5}	-5.01	2	1923	0.00	4.43	4.32	0.08
4.63×10^{-4}	0.00	-5.39	2	1923	0.00	4.43	9.39	0.03
2.44×10^{-3}	1.63×10^{-4}	-5.53	2	1923	0.00	4.43	11.31	0.01
			Chidester et al., 2017					
1.08×10^{-1}		-2.91	67	4700	0.00	0.00	20.25	2.90
1.49×10^{-1}		-3.46	61	5000	0.00	0.00	27.54	3.19
7.02×10^{-2}		-2.44	57	3800	0.00	0.00	29.91	2.01
9.74×10^{-1}		-1.63	55	5400	15.01	0.00	12.14	8.03
2.66×10^{-1}		-3.31	57	4800	0.00	0.00	23.29	0.91
5.82×10^{-2}		-3.25	41	4000	0.00	0.00	31.50	0.73
2.87×10^{-1}		-2.08	54	4400	2.74	0.00	5.13	6.86
			Blanchard et al., 2017					
2.27×10^{-1}		-0.66	62	3600	8.76	0.00	1.43	10.17
1.10×10^{-1}		-0.84	49	3500	4.13	0.00	1.10	6.79
2.99×10^{-1}		-0.66	70	3700	8.08	0.00	1.23	10.41
3.18×10^{-1}		-0.74	81	4000	10.39	0.00	2.71	12.11
2.34×10^{-1}		-0.96	49	3700	0.00	0.00	5.78	9.14
3.20×10^{-1}		-0.95	71	4000	4.12	0.00	1.60	9.20
1.34×10^{-1}		-0.83	54	4000	5.19	0.00	1.74	7.73
4.84×10^{-1}		-0.93	60	3800	0.00	0.00	3.12	10.54
3.25×10^{-1}		-0.85	71	4100	0.00	0.00	3.45	12.38
			Boujibar et al 2019					
3.09×10^{-5}	1.02×10^{-5}	-2.58	1	1973	0.61	4.09	2.91	0.12
8.91×10^{-5}	2.40×10^{-5}	-2.65	1	1853	3.21	0.76	3.79	0.23
2.95×10^{-4}	1.70×10^{-4}	-2.80	1	1823	2.31	0.62	4.20	0.19
5.25×10^{-4}	7.08×10^{-5}	-3.16	1	1973	0.50	1.88	12.02	0.06
2.09	1.48×10^{-1}	-3.16	1	1973	32.79	1.77	0.16	0.46
6.92×10^{-5}	9.77×10^{-5}	-3.20	1	1773	2.08	0.74	4.00	0.25
3.31×10^{-5}	8.32×10^{-6}	-3.59	1	1973	0.50	1.61	11.56	0.11
2.09	1.38×10^{-1}	-3.59	1	1973	33.32	1.82	0.13	0.16

3.89×10^{-5}	1.02×10^{-3}	-3.90	5	2173	1.68	1.90	14.43	0.06
2.51	1.32×10^{-1}	-3.90	5	2173	31.53	0.00	1.54	4.85
6.17×10^{-4}	1.10×10^{-4}	-4.29	1	1973	0.12	2.70	10.33	0.02
5.01×10^{-3}	8.32×10^{-6}	-5.23	1	1973	0.04	--	25.42	0.55

Appendix C. Calculation of coefficients from equation 4 for U and Th.

To determine the best parameterization of the behavior of Uranium and Thorium considering the database available, we performed a stepwise regression to determine the most pertinent variables to include in our parameterization and their best-fit parameters.

We first listed all the variables with a potential influence on the U and Th partition coefficients. In addition to the variables present in the final parameterization (Table 2), we also tested the metallic C, Ni and Si concentration and the SiO_2 concentration in the silicate. These parameters are available for all experiments in Appendix B.

Prior to each regression, we ran a correlation analysis to avoid using redundant variables. We calculated the Pearson correlation coefficient (r) for each pair of variables described here. The Pearson correlation coefficients of all variables used in the final parameterizations are listed in Table C.1. We also calculated the determination coefficient ($\hat{r}$), presented in Table C.2, which quantify the proportion of linear variance of one variable that can be explained by the other variable. In our dataset, only a few noticeable correlations can be found between the variables used in the parameterizations. The most important correlation was found between SiO_2 in the silicate and Si in the metal (r = 0.82, $\hat{r}$ = 0.67). We therefore decided to test these variables in separate regressions. For the rest of the variables, the fact that no correlations were found in our database can be explain by the diversity of the experimental conditions (P, T, fO_2) and the variety of starting compositions used by the different authors, which renders variables that are usually correlated in natural systems uncorrelated here.

a)

$log(D_U)$	$log(fO_2)$	$1/T$	$log(1-X_S)$	$log(1-X_O)$
$log(fO_2)$	1.00			
$1/T$	-0.27	1.00		
$log(1-X_S)$	0.38	-0.29	1.00	
$log(1-X_O)$	-0.31	0.19	-0.29	1.00

b)

$log(D_{Th})$	$log(fO_2)$	$1/T$	$log(1-X_S)$	$log(1-X_O)$
$log(fO_2)$	1.00			
$1/T$	-0.29	1.00		
$log(1-X_S)$	0.29	-0.35	1.00	
$log(1-X_O)$	-0.31	-0.04	0.30	1.00

Table C.1. Pearson correlation coefficients (r) for each pair of variables used in the final parameterization of a) D_U and b) D_{Th}.

a)

$log(D_U)$	$log(fO_2)$	$1/T$	$log(1-X_S)$	$log(1-X_O)$
$log(fO_2)$	1.00			
$1/T$	0.08	1.00		
$log(1-X_S)$	0.14	0.08	1.00	
$log(1-X_O)$	0.09	0.04	0.08	1.00

b)

$log(D_{Th})$	$log(fO_2)$	$1/T$	$log(1-X_S)$	$log(1-X_O)$
$log(fO_2)$	1.00			
$1/T$	0.08	1.00		
$log(1-X_S)$	0.09	0.13	1.00	
$log(1-X_O)$	0.10	0.00	0.09	1.00

Table C.2. Determination coefficients ($\hat{r}$) for each pair of variables used in the final regressions for a) U and b) Th. $\hat{r}$ is the square product of the Pearson correlation coefficient, r, which quantifies the proportion of linear variance of one variable that is explained by the other variable. The low $\hat{r}$ values presented here suggest the absence of multi-collinearity in our model.

Regressions were performed for every non-redundant variable. For each regression, the overall model significance was determined with a Fisher-Snedecor test (F value and associated p-value), and a Student's t-test was run for every single variable (t-stat and associated p-value). We used a significance level of $\alpha = 5\%$, meaning that any value associated with a p-value < 0.05 and a t-stat > 1.96 is considered to be of statistical significance, at the 95% confidence level. Every variable found to be statistically insignificant was set to 0 and the remaining variables were regressed another time. For each new regression, potential correlations of the remaining variables were checked before calculation. In the end, we obtained a regression with six statistically significant and uncorrelated variables (other than *cst*) to constrain the evolution of D_{Th} and D_U.

We first ruled out of the parameterization terms related to SiO_2 in the silicate and Ni in the metal, which were found to be of no statistical significance. We then removed the variables related to C and Si in the metal from the regression process: although they are found to be significant variable while having a weak effect, we realized parameterization with and without these parameters and the overall model robustness increased for both U and Th parameterizations when these parameters are not taking into account. The coefficients of other variables remained unchanged. Furthermore, considering the absence of any major effect on samples within graphite capsules and our qualitative analyses of metallic C in samples (obtained from the deviation of microprobe totals from 100%), we removed C in the metal from the final parameterizations.

The effect of pressure on D_{Th} is poorly constrained by the available dataset (c_{Th} = 276 ± 289, with a *p*-value of 0.54 and *t*-stat = 1.02 in the first parameterization), and, while the value of c_u is shown to be of statistical significance (c_U = 15.6 ± 45.2, with a *p*-value of 0.04 and *t*-stat = -2.52) it remains fairly negligible and overlaps with 0, within the error bar. By plotting the D_{Th}/D_U ratio versus pressure (Fig. 4), we found that this ratio is constant within uncertainties. We therefore decided to fix the parameter c_{Th} and c_U equal to 0, reducing the number of variables in the two parameterizations (other than *cst*) to four, without any effect on the other variables.

The final parameterizations of log D_U and log D_{Th} present fairly robust overall model significance. 85% and 82% (R^2) of the respective variations of log D_U and log D_{Th} observed within the data are accounted for by the variables included in the final parameterization. The Fisher-Snedecor test values of each model (96.76 for U and 35.65 for Th) associated to its *p*-value (significance *F*) confirm the overall pertinence of these parameterizations. The significance of each variable used in these models is also confirmed by their calculated *p*-values.

Final parameterization of logD_U					
Regression Statistics					
Multiple *R*	0.92				
R^2	0.85				
Adjusted R^2	0.83				
Standard error	0.67				
Observations	74				
Variance Analysis					
	degrees of freedom	*Square Sum*	*Mean Sum*	*F-value*	*Significance F*
Regression	4	182.46	45.61	96.76	$9.24 .10^{-28}$
Residual	70	32.99	0.47		
Total	74	215.45			
	Coefficients	*Standard errors*	*t-Stat*	*p-value*	
cst	-1.52	0.05	-2.94	0.004	
a	-0.72	0.10	-9.69	$1.44 .10^{-14}$	
b	-8346	1103	-8.29	$5.26 .10^{-12}$	
d	-15.3	1.10	-13.50	$3.61 .10^{-21}$	
f	-51.5	7.80	-6.55	$7.85 .10^{-9}$	

Final parameterization of logD_{Th}					
Regression Statistics					
Multiple *R*	0.88				
R^2	0.82				
Adjusted R^2	0.76				
Standard error	0.71				
Observations	44				
Variance Analysis					
	degrees of freedom	*Square Sum*	*Mean Sum*	*F-value*	*Significance F*
Regression	4	72.87	18.21	35.65	$1.53 .10^{-12}$
Residual	39	19.92	0.51		
Total	43	92.79			
	Coefficients	*Standard errors*	*t-Stat*	*p-value*	
cst	0.77	1.10	0.24	0.80	
a	-0.96	0.10	-3.20	0.002	
b	-9967	2618	-5.01	$7.22 .10^{-6}$	
d	-13.7	1.40	-9.79	$4.60 .10^{-12}$	
f	-137.8	26.6	-6.15	$2.12 .10^{-5}$	

Table C.3. Details of the regressions of equation (4) and associated significance tests.

Appendix D. (Th/U) value in EH and EL Chondrites.

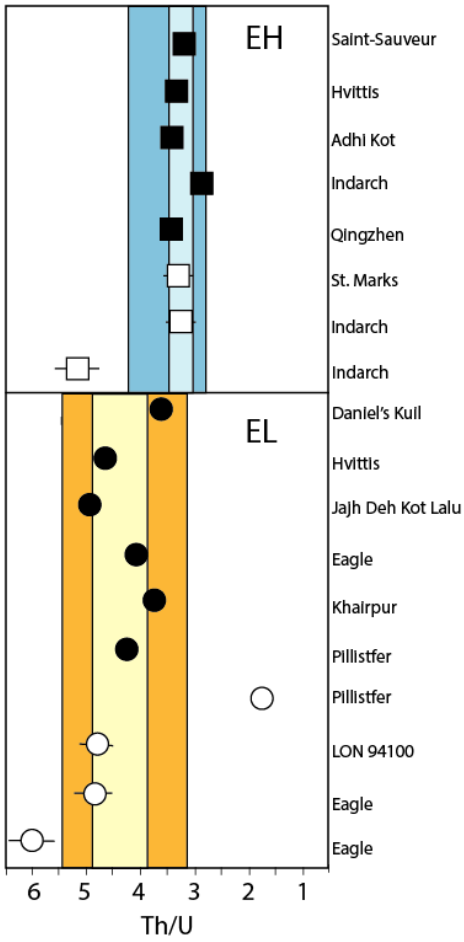

Figure S1: Th/U measured in fall EH and EL chondrites. Data from Dauphas and Pourmand (2015) (plain symbol) and Barrat et al. (2014) (open symbol). U and Th concentrations are obtained using isotope dilution measurements in Dauphas and Pourmand (2015) and classical ICPMS technique measurements in Barrat et al., (2012), with a precision on U/Th ratio of 2.4% and 7.15% (2stdev), respectively. To determine these errors, we have considered the replicate measurements published for chondrites using the same analytical techniques. Seven measurements of the carbonaceous chondrite Allende were published in Pourmand and Dauphas (2010). They obtain a precision of 2.4% (2stdev) on Th/U (3.77±0.09). Barrat et al. (2012) published 6 measurements on Orgueil (carbonaceous chondrite). They obtained precision of 7.15% (2stdev) on Th/U (3.57±0.25). These error bars are represented in the figure. They are always smaller than the symbol size for data published by Dauphas and Pourmand (2015). Among the data represented in this plot, 3 samples are significantly outside the error bar (dark blue and orange rectangle, for EH and EL chondrites, respectively), which have been removed from the dataset. The resulting Th/U average values are significantly different: $(Th/U)_{EH}$=3.24±0.17 and $(Th/U)_{EL}$=4.39±0.52 (light blue and orange fields, respectively).

Barrat, J.A., Zanda, B., Moynier, F., Bollinger, C., Liorzou, C., and Bayon, G. (2012). Geochemistry of CI chondrites: Major and trace elements, and Cu and Zn Isotopes. Geochim. Cosmochim. Acta *83*, 79–92.

Barrat, J.A., Zanda, B., Jambon, A., and Bollinger, C. (2014). The lithophile trace elements in enstatite chondrites. Geochim. Cosmochim. Acta *128*, 71–94.

Dauphas, N., and Pourmand, A. (2015). Thulium anomalies and rare earth element patterns in meteorites and Earth: Nebular fractionation and the nugget effect. Geochim. Cosmochim. Acta *163*, 234–261.

Pourmand, A., and Dauphas, N. (2010). Distribution coefficients of 60 elements on TODGA resin: Application to Ca, Lu, Hf, U and Th isotope geochemistry. Talanta *81*, 741–753.